International Journal of Heat and Mass Transfer 233 (2024) 125904

Contents lists available at ScienceDirect

International Journal of Heat and Mass Transfer

journal homepage: www.elsevier.com/locate/hmt

Buoyancy-driven circulation and multi-component mixing using SPH with a new adiabatic boundary condition

Georgina Reece[1], Benedict D. Rogers [*], Georgios Fourtakas, Steven Lind[2]

School of Engineering, University of Manchester, Manchester, UK

ARTICLE INFO

Keywords:
SPH
Buoyancy
Heating
Circulation
DualSPHysics

ABSTRACT

Multi-component fluid mixing by buoyancy-driven circulation is a common engineering process. Buoyancy-driven flows have been studied extensively using mesh-based Eulerian methods, but challenges remain especially near the fluid component interface. Smoothed particle hydrodynamics (SPH) is a meshless Lagrangian method able to deal with large deformations and a changing interface between the fluid components. Herein, an SPH formulation is proposed by employing the Boussinesq approximation to model buoyancy-driven flows where the temperature evolves by a governing equation, as well as multiple components with variable viscosities. In addition, a new implementation of an adiabatic boundary condition in SPH is included by adapting the recently developed modified dynamic boundary condition. The SPH results are compared against reference solutions for 2-D and 3-D, single and multi-component cases such as a differentially heated cavity and a cylindrical tank. Agreement is found with reference solutions for differentially heated cavity cases, provided the ratio of smoothing length to particle size is sufficiently large. Furthermore, the combined volume fraction - finite time Lyapunov exponent mixing measure gives insight into the relative movement of components at both a local and global level.

1. Introduction

Many industrial processes take advantage of convective flows for mixing, maintaining homogeneity or heating. The production of foods, polymers and glasses all employ knowledge and understanding of the thermally-driven flows involved. Buoyant convection arises where there is a difference in density within the fluid, for example due to temperature or concentration, which then induces a flow. This introduces extra features to the physical processes including natural convection, flow instabilities and turbulence.

Buoyancy-driven flows have been studied experimentally, analytically, and/or numerically for decades, including seminal work by GI Taylor, GK Batchelor and co-workers [1–3], as well as more recent studies, for example on buoyancy-driven turbulence [4] and exchange flows [5]. However, despite this progress, there are multiple cases where different simulation techniques are required such as mesh-based methods that employ direct numerical simulation [6] and large eddy simulation [7]. In particular, the flows in differentially-heated cavities with mixing of different components are used in multiple process industries (food, chemicals, pharmaceutical drugs and product mixing). Due to the confinement of the flow and the complex geometries, it is rarely possible to obtain accurate measurements of fluid properties within the container leaving numerical simulation to offer insight into such buoyancy-driven processes. However, there are still challenges predicting such buoyancy-driven flows, particularly those involving rapid phase changes.

The behaviour of buoyancy-driven flows is characterised by the Rayleigh number,

$$\mathrm{Ra} = \frac{g\beta}{\nu\kappa}\Delta\theta L^3, \tag{1}$$

where g is acceleration due to gravity, β is the coefficient of thermal expansion, ν is kinematic viscosity, κ is thermal diffusivity, $\Delta\theta$ is the temperature difference and L a characteristic length. This can be used to identify the buoyant flow regime. When changes in the density can be neglected and the fluid can be assumed to be incompressible (or weakly compressible), and all other fluid properties are constant within the range of temperatures applied, a common way of modelling buoyancy-driven flow is to use the Boussinesq approximation with an extra body force term. This approach has been used extensively for simulations (e.g. CFD simulations of laser melting [8]).

* Corresponding author.
E-mail address: benedict.rogers@manchester.ac.uk (B.D. Rogers).
[1] Present address: National Nuclear Laboratory, Warrington, UK.
[2] Present address: School of Engineering, Cardiff University, Cardiff, UK.

https://doi.org/10.1016/j.ijheatmasstransfer.2024.125904
Received 4 February 2024; Received in revised form 16 May 2024; Accepted 27 June 2024
Available online 29 July 2024
0017-9310/© 2024 The Author(s). Published by Elsevier Ltd. This is an open access article under the CC BY license (http://creativecommons.org/licenses/by/4.0/).

For the simulation of buoyancy-driven flows, mesh-based methods have been used extensively for predicting mixing [6,7]. To date, Eulerian methods have generally been preferred, since the accuracy of Lagrangian mesh-based methods is reduced when the mesh is subject to large deformations [9]. Increasing the resolution to mitigate against this can lead to an impractically small timestep [9], whilst re-meshing is highly computationally expensive. Additionally, each re-mesh introduces an error which contributes to diffusion of the material properties [9]. Therefore, fixed grid methods are typically preferred, since they do not suffer issues with deformation, though can be difficult to apply to complex geometries. Where there are multiple components, a very high resolution is required to resolve the interface with sufficient accuracy, e.g. [10]. Alternatively, interface tracking and reconstruction [11] formulations may be employed, but introduce additional computational cost. Hybrid methods, involving mapping between an Eulerian and a Lagrangian grid, aim to combine the benefits of both approaches. However, the additional layer of computation can introduce instability and reduce accuracy [9]. Moreover, it is not possible to follow a material point precisely nor predict the location of the interface between difference phases or components.

Meshless methods are able to deal with some of the limitations of mesh-based methods, and after a period of intense development are now maturing to challenge the widespread use of mesh-based schemes. In particular for this work, large deformations do not require expensive re-meshing, and moving interfaces can be followed without additional computation or reconstruction, since particles belong to a particular component phase. Most meshfree methods are Lagrangian, with computation points moving with the flow [12], but there are also Eulerian approaches with fixed particles [9]. Hybrid methods, such as particle in cell [13], also exist, where a background mesh is used along with particles. Any hybrid meshless-mesh based methods still suffer from the disadvantages of generating and/or updating a mesh.

Smoothed particle hydrodynamics (SPH) is a Lagrangian discretisation scheme, originally developed in 1977 by Gingold and Monaghan [14] as well as Lucy [15] for astrophysical modelling, but now used in a number of areas including fluid dynamics [16–19]. As a particle method, no grid is needed [20] and the particle-based formulation of SPH makes it particularly well-suited for modelling fluids with a constantly changing interface between components undergoing large deformations. It is also well-suited to modelling fragmentation in continuity of components [16], or a self-intersecting interface [18,19,21–23] even when high levels of strain are involved [16].

SPH has been applied to a number of mixing processes in industry, for example in the production of foods, pharmaceuticals or polymers. These processes tend to be mechanically-driven, since SPH is better able to manage a moving boundary than a meshed method, and target homogeneity of the end-product. Robinson and Cleary [24,25] modelled a two-dimensional twin-cam mixer using single-component SPH. Comparisons with experiments were made by computing a finite time Lyapunov exponent field to determine whether the location of manifolds in the flow agreed with the distribution of tracer dye [25].

A governing equation for temperature was first introduced by Monaghan [20], before Cleary [26] developed a more sophisticated form, which is commonly used today. Cleary and Monaghan [27] developed one of the first models for thermal conduction using SPH, improving on a previous method for thermal conduction in stars [28]. The improvements allowed for variation in the conductivity, whilst maintaining continuity of the heat flux [27]. The method was demonstrated to perform well for thermal conduction in solid domains [27].

Similar to other computational techniques, buoyancy-driven flow is typically modelled in SPH through the Boussinesq approximation [26,29,30], coupled with the temperature governing equation, including in incompressible SPH [31] since the approximation states density only varies in the Boussinesq term. Leroy et al. [31] found good agreement with mesh-based methods for Poiseuille flow, but struggled to reproduce the local Nusselt number in regions with high temperature gradients. This was attributed to the error in SPH gradient approximations [31]. Related problems were found with the convective flow case in Section 3.4.

SPH has been used to model heat transfer over longer periods of time when modelling the growth of semiconductor crystals [32]. In order to increase the time step size, and therefore reduce computation time, an implicit time integration scheme was employed [32]. It was shown that SPH was able to compete with finite volume (FV), both in terms of results and simulation time [32]. Ng et al. [33] used the Adami et al. [34] ghost boundary method with a Dirichlet condition for temperature to model heat transfer through a wall. This was preferred to a Moving Least Squares (MLS) method with mirroring, which does not retain its higher order of accuracy once particles are disordered and is more computationally expensive than SPH [33]. Sikarudi and Nikseresht [35] also found MLS to be more sensitive to disordered particles than SPH when modelling heat conduction.

For thermal boundary conditions, Dirichlet or Neumann boundary conditions may be used [36]. For a Dirichlet condition, any boundary particles can simply be given the prescribed boundary value. A straightforward way of approximating a homogeneous Neumann condition (adiabatic for temperature) is to exclude boundary particles from the SPH summation [27]. However, this truncates the kernel near the boundary and can lead to problems similar to those outlined above for dummy particles. Alternatively, the values in the fluid may be reflected across the boundary whilst keeping the same sign [37]. On the other hand, using the negative of the fluid value in the boundary gives the homogeneous Dirichlet condition [37], where the value is zero at the boundary (for example, no-slip velocity). This method can increase the accuracy of Laplacian term approximations near the boundary [38].

For a heterogeneous Neumann boundary condition the flux across the boundary must be prescribed, which is more complicated to implement in SPH. For example, the unified semi-analytical wall boundary approach [39] uses an extrapolation onto boundary particles, so that the segment between these points has the mean value of the flux, to produce a first-order Neumann boundary condition. Recently, Joubert et al. [40] applied a gradient correction at the boundary surface in order to enforce Neumann boundary conditions for pressure and velocity. Alternatively, Bai et al. [41] developed a new SPH-finite difference method (FDM) which converts a Neumann condition to a Dirichlet condition, in order for it to be applied to the SPH part of the method. Sikarudi and Nikseresht [35] introduce a new boundary method to implement an adiabatic boundary condition, which ensures no heat flux through a boundary [35]. The intuitive method of excluding boundary particles from interpolated values is unable to completely stop heat transfer due to the incomplete kernel [35].

The previous research emphasises the need for a robust adiabatic boundary treatment in SPH for application to buoyancy-driven circulation in confined domains. The open-source SPH solver DualSPHysics [42] is chosen to be adapted for this model for its current capabilities and the capacity for modification. The DualSPHysics solver is rigorously validated and widely used in both academia and industry, providing a highly optimised code that runs on different hardware including a central processing unit (CPU) or a graphics processing unit (GPU) [42]. Currently the solver does not include a governing equation for temperature or any heating effects. A multi-component option with non-Newtonian components has recently been included [42], as well as the modified Dynamic Boundary Condition (mDBC) of English et al. [43]. However, the new mDBC boundary condition is only applicable to the isothermal Navier–Stokes equations. Therefore a new adiabatic boundary condition is needed to extend its applicability to the buoyancy-driven flows considered herein. Introducing new functionality into an existing highly-optimised code presents special coding challenges. Specifically, introducing new functionality that still exploits the acceleration of the GPU without making major structural changes to the code must be achieved with minimal effect on the computational

speed. Herein, all modifications have been made to both CPU and GPU variants of the DualSPHysics code.

The new thermal boundary condition is based on an extension of the mDBC and is therefore 1st-order consistent as well as being up to 2nd-order accurate. This has therefore opened new opportunities for further applications requiring accurate and robust adiabatic SPH boundary treatments. The paper also presents the first 3-D application of the mixing measure to a complex geometry (first demonstrated in 2-D in [44]). Finally, the entire simulation has been accelerated on the GPU version of DualSPHysics, which has not been possible previously for thermal applications, thereby enabling widespread use.

This paper is structured as follows. The following section will present the governing equations and SPH methodology, including the new adiabatic boundary condition, Section 3 will present numerical results, before conclusions are presented in Section 4. The model is validated with heat conduction and differentially heated cavity cases, before being used to investigate convective flow in a cylindrical tank.

2. Numerical methodology

2.1. Governing equations

The physics of the flow are governed by the Navier Stokes equations, which include conservation of mass, momentum, and energy,

$$\frac{D\rho}{Dt} + \rho\nabla\cdot\mathbf{v} = 0; \tag{2}$$

$$\rho\frac{D\mathbf{v}}{Dt} = -\nabla p + \nabla\cdot\tau + \rho\mathbf{f}; \tag{3}$$

$$\rho\frac{DU}{Dt} = \rho\dot{q} + \nabla\cdot(k\nabla\theta) - \nabla\cdot(\mathbf{v}p) + \nabla\cdot(\mathbf{v}\tau) + \rho\mathbf{f}\cdot\mathbf{v}. \tag{4}$$

where $\frac{D}{Dt}$ is the material derivative, ρ density, $\mathbf{v}$ velocity, p pressure, τ is the extra stress tensor, $\mathbf{f}$ the body force acting on the fluid, U the internal energy, θ the temperature and $\dot{q}$ the rate of heat transfer. The fluid is assumed to be weakly compressible, and the state variables are linked through an equation of state.

2.2. SPH methodology

In the SPH method, particles (which may be irregularly spaced) are used to represent a medium. Each particle, which is a computational node, has physical properties and interacts with nearby particles, thus changing its properties [16]. To facilitate this, a particle has a domain of influence with radius proportional to the smoothing length (h) of the kernel (W) used. For an arbitrary material property Φ, the value at a point $\mathbf{r}$ is computed through the interpolation

$$\langle\Phi(\mathbf{r})\rangle = \int_{\Omega}\Phi(\mathbf{r})W(\mathbf{r}-\mathbf{r}',h)d\mathbf{r}' \tag{5}$$

over the domain Ω. The Wendland kernel [45] is chosen for this work due to its high accuracy [46]. It is a fifth-order polynomial function with compact support.

To apply to the discretised SPH domain, the function in Eq. (5) is approximated as a sum over SPH particles. The value of Φ at particle i is then summed over all particles j in the domain

$$\langle\Phi(\mathbf{r}_i)\rangle = \sum_j \frac{m_j}{\rho_j}\Phi_j W_{ij}, \tag{6}$$

where subscripts i and j denote SPH particle numbers, m_j is the mass of particle j, ρ_j its density, and Φ_j is the value of Φ at particle j. The notation is simplified in a standard way such that $W_{ij} = W(\mathbf{r}_i - \mathbf{r}_j, h)$ and the relative velocity $\mathbf{v}_{ij} = \mathbf{v}_i - \mathbf{v}_j$.

2.3. SPH formulation

The governing equations in Section 2.1 are therefore written as

$$\frac{D\rho_i}{Dt} = \rho_i\sum_j\frac{m_j}{\rho_j}\mathbf{v}_{ij}\cdot\nabla_i W_{ij}; \tag{7}$$

$$\frac{D\mathbf{v}_i}{Dt} = -\sum_j m_j\frac{p_j+p_i}{\rho_j\rho_i}\nabla_i W_{ij} + \nu\nabla^2\mathbf{v}_i + \mathbf{f}_i; \tag{8}$$

$$\frac{D\theta_i}{Dt} = \frac{1}{C_{p,i}}\sum_j\frac{m_j}{\rho_i\rho_j}\frac{4k_ik_j}{k_i+k_j}(\theta_i-\theta_j)\frac{\nabla_i W_{ij}}{r_{ij}}. \tag{9}$$

where $C_{p,i}$ is the specific heat capacity at particle i. The energy equation follows the form used by Monaghan [20], where the pressure and viscous heating terms from Eq. (4) are neglected due to the assumption of weak compressibility. Temperature is chosen as a material variable to give to particles, rather than internal energy, for application of initial conditions and interpretation of results. This is accomplished through the directly proportional relationship between internal energy and heat, with the coefficient specific heat constant. The Wendland kernel [45] used in this work is defined as

$$W(\mathbf{r_{ij}},h) = \begin{cases}\frac{7}{4\pi h^2}\left(1-\frac{r_{ij}}{2h}\right)^4\left(\frac{2r_{ij}}{h}+1\right) & r_{ij}\in[0,2h],\\ 0 & \text{otherwise.}\end{cases} \tag{10}$$

where $\mathbf{r}_{ij} = \mathbf{r}_i - \mathbf{r}_j$ and $r_{ij} = |\mathbf{r}_{ij}|$.

The equation of state commonly known as Tait's equation is used [16]:

$$p = B\left[\left(\frac{\rho}{\rho_0}\right)^{\gamma} - 1\right]. \tag{11}$$

Here B is a constant, $\gamma \in [1,7]$ (chosen to be 7 unless otherwise specified) is a constant known as the polytropic index of the fluid, and ρ_0 is the reference density (chosen to be initial density) [47].

2.4. Viscous diffusion

To accommodate interacting particles with different viscosities, a viscous term is used which takes the average of the two viscosities involved. In previous work [44], the viscous formulation of Morris et al. [48] is modified by using the arithmetic mean of both viscosities involved in the interaction, such that

$$\nu\nabla^2\mathbf{v}_i = \sum_j m_j\frac{2(\nu_i+\nu_j)}{\rho_i+\rho_j}\left(\frac{\mathbf{r}_{ij}\cdot\nabla_i W_{ij}}{\mathbf{r}_{ij}^2+\eta^2}\right)\mathbf{v}_{ij}. \tag{12}$$

The viscous term in Eq. (8) is equivalent to the stress tensor term in Eq. (3) for incompressible Newtonian fluids, assuming that viscosity is constant and independent of other variables. However, for this work viscosity is not always constant in the whole domain. Note, if the Stokes' hypothesis is dropped and the bulk viscosity term reinstated then

$$\nabla\cdot\tau = \nu\nabla^2\mathbf{v} + \left(\nu+\frac{\lambda}{\rho}\right)\nabla(\nabla\cdot\mathbf{v}), \tag{13}$$

where bulk viscosity is equal to $\frac{2}{3}\mu+\lambda$, as determined by Bonet-Avalos et al. [49] with μ being the dynamic viscosity and λ being the second coefficient of viscosity.

For this work, the constant viscosity is replaced with the average viscosity of the two interacting particles, as in Eq. (12), so that

$$\nu\nabla^2\mathbf{v}_i = \sum_j m_j\frac{2(\nu_i+\nu_j)}{\rho_i+\rho_j}\left(\frac{\mathbf{r}_{ij}\cdot\mathbf{v}_{ij}}{\mathbf{r}_{ij}^2+\eta^2}\right)\nabla_i W_{ij}. \tag{14}$$

The advantages of using this Monaghan and Gingold [50] operator above are considered for the differentially heated cavity case in Section 3.2.

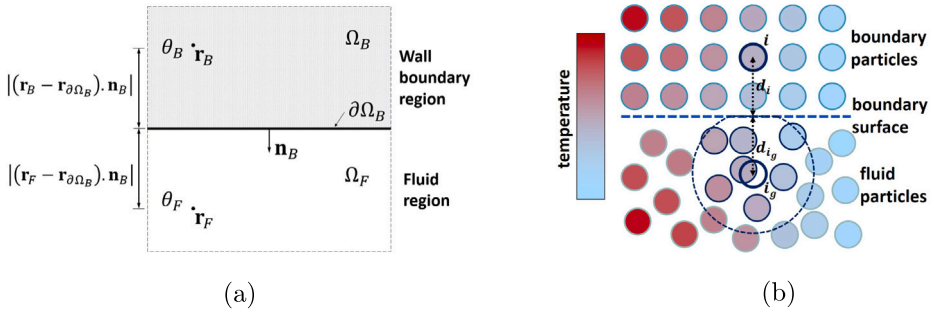

Fig. 1. The adiabatic boundary condition is enforced by reflecting fluid temperatures across the boundary line onto boundary particles. (a) Continuous domain: Sketch of fluid region Ω_F and solid wall boundary region Ω_B with boundary location $\partial\Omega_B$. The wall normal $\mathbf{n}_B$ is defined as pointing away from the solid boundary into the fluid region. The thermal mDBC defines the wall boundary temperature θ_B at a location $\mathbf{r}_B$ as a function of the fluid temperature θ_F at mirror location $\mathbf{r}_F$ using perpendicular distance from $\partial\Omega_B$ as $\theta_B = \theta(|(\mathbf{r}_B - \mathbf{r}_{\partial\Omega_B}) \cdot \mathbf{n}_B|) = \theta(|(\mathbf{r}_F - \mathbf{r}_{\partial\Omega_B}) \cdot \mathbf{n}_B|)$, (b) Discrete domain: Boundary particle i temperature is interpolated at ghost particle i_g for new adiabatic boundary condition based on mDBC.

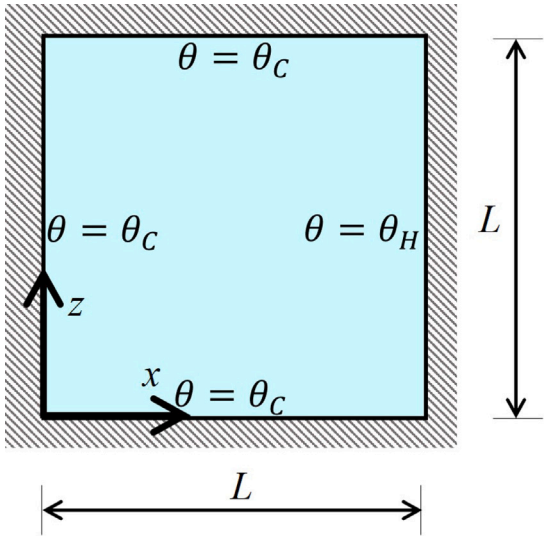

Fig. 2. Diagram of cavity for heat conduction case.

2.5. Thermal buoyancy

For natural convection, the body force acting on the fluid is due to gravitational acceleration. The Boussinesq approximation states that, assuming variations in other properties with temperature are small, changes in fluid density may be neglected in the governing equations, except in the body force term. The approximation of the body force is derived from a first-order Taylor series of density as a function of temperature about a reference temperature θ_0. Then the body force acting on the fluid in the conservation of momentum, Eq. (3), becomes

$$\mathbf{f}_i = -\mathbf{g}\beta(\theta_i - \theta_0). \tag{15}$$

where $\mathbf{g}$ is the gravity vector. In this way, the momentum equation and energy equation are coupled. This form is used in many mixing models [30,33,51,52].

2.6. New adiabatic boundary condition

The fluid is heated by applying a Dirichlet condition to the boundary, such that

$$\theta = \theta_B \tag{16}$$

is constant for some boundary temperature θ_B.

An adiabatic boundary (no heat transfer) can be approximated by setting the thermal conductivity to

$$k = 0 \tag{17}$$

for the boundary component, so that particles in this component do not contribute to the temperature evolution in Eq. (9). This is equivalent to the naturally adiabatic condition of no boundary particles for solids described by Cleary [26], giving a zeroth order approximation, so is expected to have similar limitations. This approach introduces additional truncation error, since the kernels of fluid particles near the boundary are incomplete when computing a change in temperature. However, the existing boundary particles are able to contribute to SPH summations for other variables, so no additional truncation error is introduced here.

For a homogeneous Neumann condition (such as an adiabatic boundary for temperature) the symmetric boundary condition can be used as shown in Fig. 1. A more accurate approach than Eq. (17) can be derived by extending the first-order consistent mDBC method, recently introduced by English et al. [43] for density. The mDBC treatment is a modification to the DualSPHysics dynamic boundary condition (DBC) based on the work of Marrone et al. (2011) [53], which reduces penetration of boundaries as well as allowing for partial slip conditions. Layers of boundary particles are used, as with DBC, but the physical boundary is midway between fluid and boundary particles. Boundary particles are mirrored into the fluid as ghost particles along the boundary normal into the fluid. At corners boundary particles are reflected onto ghost particles along a line through the vertex. Density and its gradient are found at a boundary particle i for its corresponding ghost particle i_g using SPH interpolation over surrounding fluid particles, along with the first-order consistent correction of Liu and Liu [54]. When there are too few particles within the kernel of the ghost particle, the correction is not possible and a Shepard filter is used instead. Density at a boundary particle i is then calculated through

$$\rho_{i_g} = \rho_i + (\mathbf{r}_i - \mathbf{r}_{i_g}) \cdot \begin{bmatrix} \partial_x \rho_i \\ \partial_y \rho_i \\ \partial_z \rho_i \end{bmatrix}. \tag{18}$$

Boundary particles are given zero velocity, unless a moving boundary is specified, as for the DBC method. No-slip boundary conditions are enforced by setting boundary particle velocities to $\mathbf{v} = (0, 0)$.

Following the mDBC method for computing normals and ghost particles, the temperature at a boundary particle i is the temperature interpolated at its corresponding ghost particle i_g. As with density, the correction of Liu and Liu [54] is applied to θ_{i_g} as shown in Fig. 1, then

$$\theta_i = \theta_{i_g}. \tag{19}$$

This is the same as Eq. (18) without the gradient term. In this way, temperature is reflected onto boundary particle across the line of the adiabatic boundary, blocking heat transfer through the boundary.

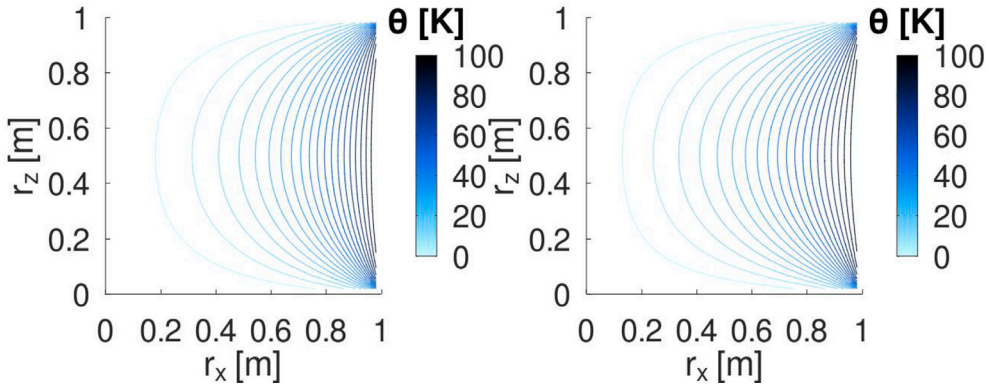

Fig. 3. Comparison of isotherms for heat conduction case: SPH model on left, analytical solution on right.

The introduction of the mDBC method [43] has created opportunities for more accurate boundary conditions for other flow properties. The new thermal boundary condition in this paper exploits the up to 2nd-order accuracy and 1st-order consistency of mDBC. Similar ideas have been explored in [12] who used a zeroth-order correction and linear extrapolation centred on mapping particles located at the boundary for vertical walls. However, the approach presented herein is suitable for general application and ensures 1st-order consistency as well as avoiding kernel truncation errors. It is demonstrated here that it allows the simulation of the physical processes of 3-D thermal flows with linear consistency at the adiabatic walls, with both CPU and GPU implementations.

2.7. Timestepping and timestep size

Along with the two timestep size criteria included in DualSPHysics [42] (which account for acceleration, $\mathbf{a}$, and speed of sound, c), defined as

$$dt_f = \sqrt{\frac{h}{|\mathbf{a}|_{\max}}} \tag{20}$$

$$dt_c = \frac{h}{\max\left\{c, 10|\mathbf{v}|_{\max}\right\} + h\bar{\nu}}, \tag{21}$$

where $\bar{\nu}$ is the lower of the viscosities present, the criterion accounting for viscous dissipation, added to DualSPHysics by Fourtakas and Rogers [55], is used

$$dt_\nu = \frac{h^2}{\nu_{\max}\lambda_r}, \tag{22}$$

where λ_r is a relaxation parameter set for each case. For this work, with each SPH particle having its own viscosity, $\nu_{\max}$ is taken to be the maximum viscosity of all particles as interaction forces are computed in each timestep.

Additionally, a fourth timestep constraint must account for thermal dissipation when temperature evolution (Eq. (9)) is included in the model. Cleary [26] introduced the diffusion timestep criterion due to heat transfer for SPH:

$$dt_\theta \leq \frac{0.1\rho C_V h^2}{k}, \tag{23}$$

where the coefficient 0.1 corresponds to a Courant-type number. This work uses specific heat at constant pressure, rather than constant volume. Although $C_p > C_V$, the difference is small relative to their magnitudes so will not have a significant effect on the timestep size. A thermal time constraint parameter can be defined as

$$\Theta_i = \frac{k_i}{\rho_i (C_p)_i} \tag{24}$$

Since k, C_p can vary between components and density varies with time and between particles, $\Theta_{\max} = \max_i \Theta_i$ is computed at each timestep as $\nu_{\max}$ and the final timestep constraint is

$$dt_\theta = 0.1\frac{h^2}{\Theta_{\max}}. \tag{25}$$

The resultant timestep chosen for each time integration iteration is

$$dt = C_0 \min\{dt_f, dt_c, dt_\nu, dt_\theta\}, \tag{26}$$

where C_0 is the chosen CFL number. A lower limit to dt is typically set as

$$dt_{\min} \leq 0.05\frac{h}{c}, \tag{27}$$

or may be chosen explicitly, in order to avoid the timestep becoming prohibitively small.

Multiple components are included in order to be able to simulate mixing driven by the convective flow. The non-Newtonian multi-components code of Fourtakas and Rogers [55] is adapted for components of different viscosity. It is also extended to admit boundary components, so that boundary conditions may be assigned in this way as a separate component, as for the adiabatic boundary condition.

2.8. Implementation in DualSPHysics

The DualSPHysics code is a highly optimised open-source SPH code designed to run simulations exploiting the hardware acceleration provided by graphics processing units (GPUs).

Currently, DualSPHysics admits a single viscosity for a simulation. Arrays have been added to the code so that each SPH particle may have its own viscosity and temperature. Both are included as global arrays within DualSPHysics, so they can be accessed and updated at any point during the simulation, as well as output to files.

An option flag is added to choose to set multiple components with different viscosities and thermal properties. When setting up a case, component parameters and options are assigned within the special section of the case XML input file. Each component is identified by a unique number, which is stored along with its component properties. The same properties can be allocated to boundaries in order to set boundary conditions.

Initial viscosity and temperature are given to each SPH particle according to which component they lie in during the initialisation of the case. If the option flag is selected then the code forks to use particle interaction functions including the modified viscous term in Eq. (12) and temperature evolution Eq. (9). For each SPH particle, the component number is found and corresponding component properties are looked up from the component arrays to be used in the interaction equations.

Extending these modifications to the GPU code was found to speed up simulations by over 45 times. Further details of the implementation

in DualSPHysics, with a complete list of component parameter options, can be found in Section 3.4 of Reece [56].

3. Numerical results and discussion

3.1. Heat conduction validation

Firstly, the ability of the added governing Eq. (9) for temperature to produce a temperature gradient is demonstrated. The square cavity of width $L = 1$ m in Fig. 2 is filled by a fluid with constant viscosity. The fluid is discretised with particle spacing $dp = 0.02$ m, giving 50 particles across the cavity. The Boussinesq approximation is not included and gravity is set to zero as $\mathbf{g} = 0\ \mathrm{m\,s^{-2}}$, so the fluid remains approximately stationary. The speed of sound is then manually set to $c = 10\ \mathrm{m\,s^{-1}}$. The right boundary has constant temperature $\theta_H = 100$ K and the other 3 boundaries are constant at $\theta_C = 0$ K. Initially, the fluid has a uniform temperature of θ_C with thermal parameters $C_p = 100\ \mathrm{J\,kg^{-1}\,K^{-1}}$, $k = 2\ \mathrm{W\,m^{-1}\,K^{-1}}$, and has physical parameters of water $\rho = 1000\ \mathrm{kg\,m^{-3}}$, $\nu = 10^{-6}\ \mathrm{m^2\,s^{-1}}$. Its temperature is then governed by Eq. (9). Boundary particles are given the same parameter values, but have constant temperature. Density is extrapolated into the boundary using the mDBC method in Eq. (18). The resulting temperature field is shown in Fig. 3, where it can be compared with the analytical solution.

An analytical solution is found from the two-dimensional diffusion equation for temperature,

$$\frac{\partial\theta}{\partial t} = \frac{k}{C_p\rho}\nabla^2\theta = \frac{k}{C_p\rho}\left(\frac{\partial^2\theta}{\partial x^2} + \frac{\partial^2\theta}{\partial z^2}\right) \tag{28}$$

on the domain $x \in [0, L], z \in [0, L]$, with inhomogeneous boundary conditions

$$\theta(0, z, t) = 0;$$
$$\theta(L, z, t) = \theta_H = 100;$$
$$\theta(x, 0, t) = \theta(x, L, t) = \theta_C = 0.$$

Looking for steady state solution for this Dirichlet problem by separation of variables, the global solution is

$$\theta(x, z) = \sum_{n=1}^{\infty} \frac{2\theta_H}{n\pi\sinh(n\pi)}(1 - (-1)^n)\sin\left(\frac{n\pi}{L}z\right)\sinh\left(\frac{n\pi}{L}x\right). \tag{29}$$

Since for even n, $(1 - (-1)^n) = 0$; and for odd n, $(1 - (-1)^n) = 2$ the solution can be rewritten as

$$\theta(x, z) = \frac{4\theta_H}{\pi}\sum_{n=1}^{\infty} \frac{1}{(2n-1)\sinh((2n-1)\pi)}\sin\left(\frac{(2n-1)\pi}{L}z\right)\sinh\left(\frac{(2n-1)\pi}{L}x\right). \tag{30}$$

This is particularly useful numerically where the solution must be approximated as a finite sum. When computing the solution numerically, and since $\sinh(x)$ is not bounded, a finite sum must be used where N approximates infinity. $N = 100$ was found to be adequate in MATLAB.

It can be seen in Fig. 3 that the results of this SPH model compare well with the analytical solution found. The error is quantified with an L^2 norm as

$$L^2(\theta) = \sqrt{\frac{1}{\mathcal{N}}\sum\frac{(\theta_{\text{analytical}} - \theta_{\text{SPH}})^2}{\theta_H^2}} \tag{31}$$

where $\mathcal{N}$ is the total particle number, and point-wise error is approximately constant throughout the fluid domain. Fig. 4 shows the particle convergence plot for this case. It can be seen that initially the convergence rate is between first and second order before the error starts to saturate as the interparticle distance dp decreases. This convergence behaviour is typical for cases with stationary particles [57].

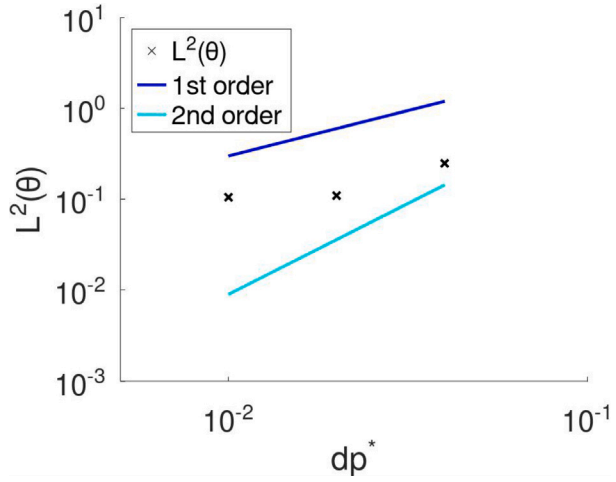

Fig. 4. Particle convergence of $L^2(\theta)$ norm with interparticle spacing dp for the heat conduction case.

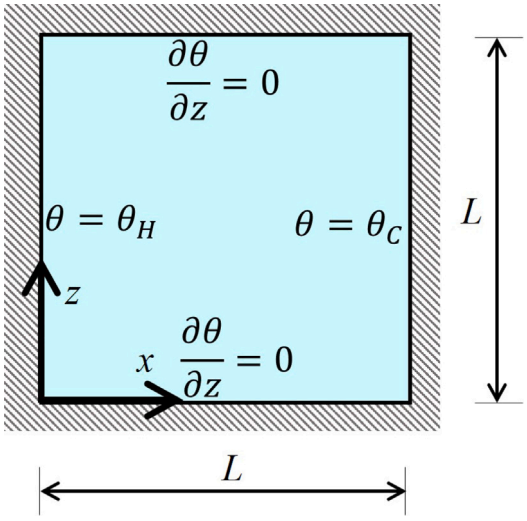

Fig. 5. Diagram of differentially heated cavity flow.

3.2. Differentially heated cavity

For this test case, the geometry is again a two-dimensional square cavity, but with the top and bottom boundary conditions being adiabatic as in Fig. 5. The literature [58,59] has the fluid filling the cavity as air at room temperature, with $Pr = 0.71$, and Ra ranging from 10^3 to 10^8 (all within the region of laminar flow [59]). In this work, the fluid is taken to be air at $\theta = 20\,^{\circ}\mathrm{C}$ and $Ra = 10^5$ chosen for comparison with data in the literature. The values used can be seen in Table 1. Following Barakos et al. [60], the temperature difference is fixed whilst the cavity width L is varied to set Ra. To ensure that the temperature difference between boundaries is large enough to have a significant effect on the flow, and any velocities are orders of magnitude larger than the size of errors, it is chosen to be $\theta_H - \theta_C = 20$ K with $\theta_H = 303$ K. This means that the cavity width must be $L = 0.0386$ m to maintain chosen characteristic values. Note that the commonly-used density reinitialisation and diffusion techniques [16,61] are not used in this approach.

Fluid is initially stationary and starts with uniform temperature $\theta(t = 0) = 293$ K, which is also set as the reference temperature (θ_0) in

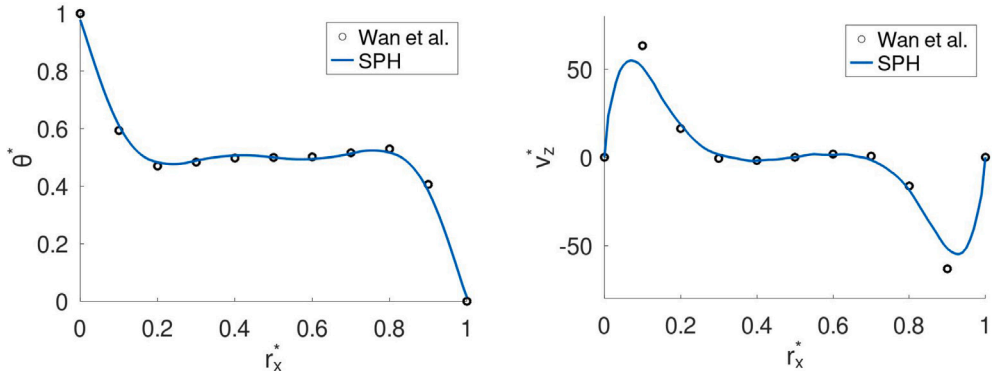

Fig. 6. Temperature (θ^*) and vertical velocity (v_z^*) along horizontal mid-line for $dp = 0.00025$ m at $t^* = 0.5$ for 2-D differentially-heated cavity.

Table 1
Parameter values for differentially heated cavity flow.

Parameter	Value
ν	1.506×10^{-5} m^2 s^{-1}
ρ	1.204 kg m^{-3}
C_p	1.006×10^3 J kg^{-1} K^{-1}
k	0.02587 W m^{-1} K^{-1}
β	3.43×10^{-3} K^{-1}
g	−9.81 m s^{-2}

Table 2
Simulation parameters for differentially heated cavity case.

h	$2dp$
c	$12\|\mathbf{v}\|_{\max}$
CFL number	0.1
Viscous term	Monaghan and Gingold [50] operator with arithmetic mean
Particle shifting type	Full
Shifting coefficient	−2
Density diffusion type	None

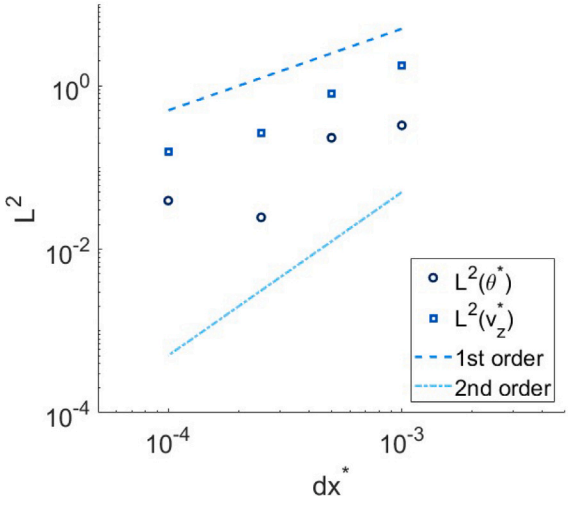

Fig. 7. Convergence of θ^* and v_z^* with increasing resolution, for $h = 2.5dp$, for the 2-D differentially heated cavity case.

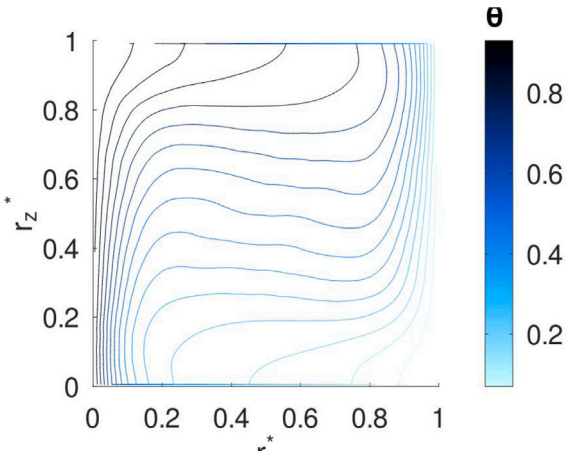

Fig. 8. Isotherms for $Ra = 10^5$ for differentially heated cavity with new mDBC adiabatic boundary condition at $t^* = 0.5$.

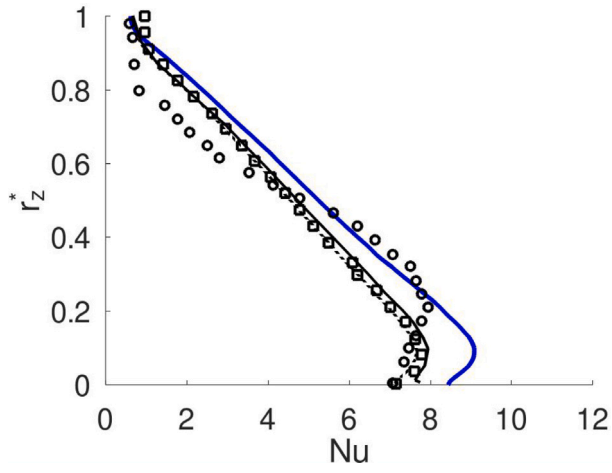

Fig. 9. Nusselt number at hot wall of differentially heated cavity for $Ra = 10^5$. Results with new mDBC adiabatic boundary condition at $t^* = 0.5$ in blue; with ∘ Massarotti et al.[62], □ Manzari [63], · Wan et al. DSC, – Wan el al. FEM. [59].

the Boussinesq term. Unlike the previous case in Section 3.1, a realistic gravitational acceleration is included in the Boussinesq term (Eq. (15)).

The key non-dimensional parameters for this case are the Prandtl number

$$Pr = \frac{\nu \rho C_p}{k}, \tag{32}$$

which gives a ratio of viscous to thermal diffusion, and the Rayleigh number

$$Ra = \frac{g\beta L^3(\theta_H - \theta_C)C_p}{\nu k}, \tag{33}$$

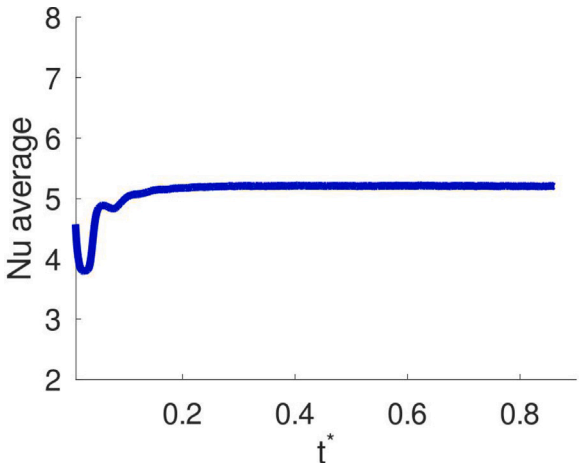

Fig. 10. Average Nusselt number at hot wall for differentially heated cavity. Plotted from $t^* = 0.01$ onwards since there is a discontinuity in temperature at the boundary for initial conditions.

Table 3
Runtime for two and three dimensions for differentially heated cavity case (to 4 significant figures) with CFL number 0.1, smoothing length $h = 2.0dp$, particle spacing 0.00025 m for 60 s.

Dimensions	Number of fluid particles	Runtime [s]
2	23 716	32 330
3	474 320	443 700

which characterises natural convection in the flow. A higher Rayleigh number indicates that buoyancy forces are more important to the flow than viscous forces.

Boundary conditions for density and velocity are imposed using mDBC, as described in Eq. (18). The boundaries are given the same parameters as the fluid in Table 1, but are stationary and not governed by Eq. (9) so do not need a value for thermal expansion coefficient, β. Instead, left and right boundaries are held at constant temperatures θ_H and θ_C respectively by assigning corresponding boundary particles these temperatures. Top and bottom boundaries are adiabatic, that is $\frac{\partial\theta}{\partial z} = 0$, and are given the same initial temperature as the fluid. This is achieved using the new adiabatic boundary method in Eq. (19) based on mDBC. Following the timestep constraint of Wan et al. [59],

$$dt \leq \min\left\{\frac{4Pr}{(|v_x| + |v_z|)^2}, \frac{Pr(dp)^2}{2}\right\} = 1.42 \times 10^{-6}, \tag{34}$$

the initial timestep size is chosen to be $dt = 1.5 \times 10^{-6}$ s.

A kernel smoothing length of $h = 2dp$ was found to be required for flow to remain in motion at steady state, demonstrating that the number of neighbouring particles is key to running this case successfully. For smaller h, numerical dissipation dominates and results in the temperature profile diffusing itself. This results in a reduction of the particle velocities such that fluid stops moving, and all heat transfer is by conduction rather than convection. Simulation parameters used for the successful differentially heated cavity cases are summarised in Table 2. Contributions to numerical dissipation come from the timestep, shifting (all particle types with coefficient $D = -2$ [66]) and the viscous term (no density diffusion is applied), as well as the SPH approximation error. The timestep constraints for viscosity and temperature (Eqs. (22) and (25)) are both included and the simulation is run with a CFL number of 0.1 and speed of sound $c = 12|\mathbf{v}|_{\max}$. The viscous term is approximated with the Monaghan and Gingold operator, using the arithmetic mean in Eq. (14).

Results are compared with those of Wan et al. [59], who use a high order discrete singular convolution scheme, for $Ra = 10^5$ at the highest resolution (161 × 161 mesh points). The SPH model is first run with a particle spacing of $dp = 0.0005$ m, which means there are approximately 77 × 77 fluid particles. Non-dimensionalised variables, denoted by *, are used for comparison and computed through [59]

$$\mathbf{r}^* = \frac{\mathbf{r}}{L};$$
$$\mathbf{v}^* = \frac{\mathbf{v}L\rho C_P}{k};$$
$$\theta^* = \frac{\theta - \theta_C}{\theta_H - \theta_C};$$
$$t^* = \frac{tk}{L^2\rho C_p}.$$

For $L = 0.0386$ m, the horizontal line through the centre of the cavity lies at $r_z = \frac{L}{2} = 0.0193$ m. Values for temperature and vertical velocity are computed at equally spaced points along this line using the SPH interpolation (Eq. (6)) of output data. Measurements are taken at time $t^* = 0.5$, which corresponds to $t = 34.88$ s, when Wan et al. [59] found the flow has reached a steady state.

Results for temperature and vertical velocity component can be seen in Fig. 6 respectively, interpolated from output data and plotted with the benchmark data of Wan et al. [59]. Due to the different boundary approaches for temperature and velocity, when plotting results, boundary particles are included in the SPH summation for temperature, but only fluid particles are included (with a kernel correction) when computing velocity. The condition for no-slip boundaries is achieved in the current version of mDBC by setting $\mathbf{v} = 0$ m s^{-1} for boundary particles. The same approach is used for no-slip DBC and is known to produce poor velocity gradients near walls. This results in non-zero velocity at the wall when boundary particles are included in the summation, and may contribute to the decrease in flow velocity found for smaller smoothing lengths.

A convergence study is undertaken with fixed $h = 2.5dp$ for varying resolution by changing particle spacing dp. Error is computed through the L^2 norms over N data points along the horizontal centre line

$$L^2(\theta^*) = \sqrt{\frac{\sum_{i=1}^{N}(\theta^*_{\text{SPH}} - \theta^*_{\text{ref}})^2}{\sum_{i=1}^{N}(\theta^*_{\text{ref}})^2}} \tag{35}$$

$$L^2(v_z^*) = \sqrt{\frac{\sum_{i=1}^{N}((v_z^*)_{\text{SPH}} - (v_z^*)_{\text{ref}})^2}{\sum_{i=1}^{N}(v_z^*)^2_{\text{ref}}}} \tag{36}$$

where subscript 'ref' denotes the value in the literature. A larger smoothing length is chosen than previously to allow the simulation to

Table 4
Mixing measures, with global measures below line.

Mixing measure	Definition
Volume fraction of phase A at point i	$F_i^A = \frac{\sum_{j\in J} V_j^2 W_{ij}}{\sum_{j\in J} V_j^2 W_{ij}}$,
Finite time Lyapunov exponent at time T [64]	$\Lambda_i(T) = \frac{\ln(d_{\max}(\mathbf{r}_i(t=0),T))}{T}$
	$d_{\max}(\mathbf{r}_i(t=0),T) = \max_j\left\{\frac{r_{ij}(t=T)}{r_{ij}(t=0)}\right\}$
Robinson's local mixing measure [24]	$M_i = (\sqrt{2}+1)\left(\frac{\frac{F_i^A}{F^A} + \frac{1-F_i^A}{1-F^A}}{\sqrt{\left(\frac{F_i^A}{F^A}\right)^2 + \left(\frac{1-F_i^A}{1-F^A}\right)^2}} - 1\right)$
New mixing measure [44]	$\overline{M} = \overline{\Lambda}\cdot\overline{F} \in [0,1]$
	$\overline{\Lambda}_i = \frac{\Lambda_i}{\max_j \Lambda_j}$
	$\overline{F}_i^A = \begin{cases} \frac{F_i^A}{F^A} & \text{if } F_i^A \leq F^A \\ \frac{1-F_i^A}{1-F^A} & \text{if } F_i^A > F^A \end{cases}$
Mixing entropy [65]	$S_A^* := \frac{S-\overline{S}}{S_{\max}-\overline{S}}$
	$S_A = -\sum_{j=1}^{N} F_j^A \log(F_j^A)$
	$\overline{S}_A = S_A(t=0)$
New mixing measure [44]	$\overline{M}^G = \frac{1}{N}\sum_{j=1}^{N}\overline{M}_j$

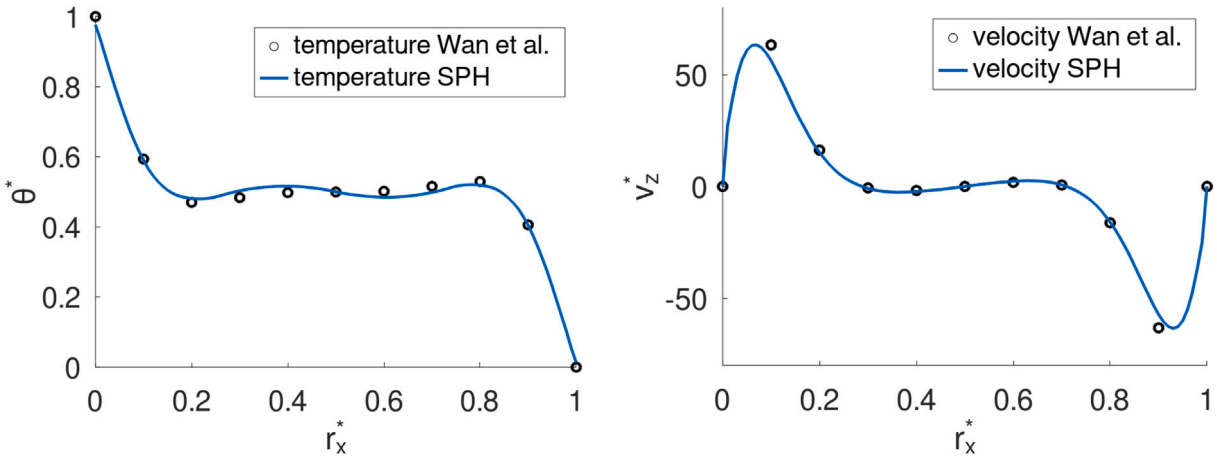

Fig. 11. Temperature (θ^*, left) and vertical velocity component (v_z^*, right) plots along a horizontal line through the centre of the cavity for the quasi-2D case, compared with the results of Wan et al. [59]. CFL number 0.1, $h = 2.0dp$, 10 particles in periodic dimension.

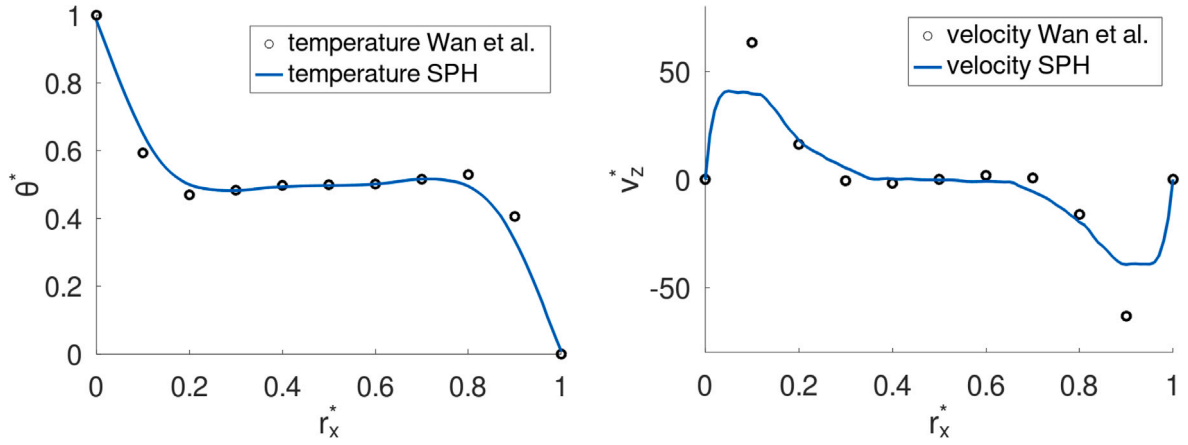

Fig. 12. Temperature (θ^*, left) and vertical velocity component (v_z^*, right) plots along a horizontal line through the centre of the cavity for the quasi-2D case, compared with the results of Wan et al. [59]. CFL number 0.2, $h = 1.5dp$, 20 particles in periodic dimension.

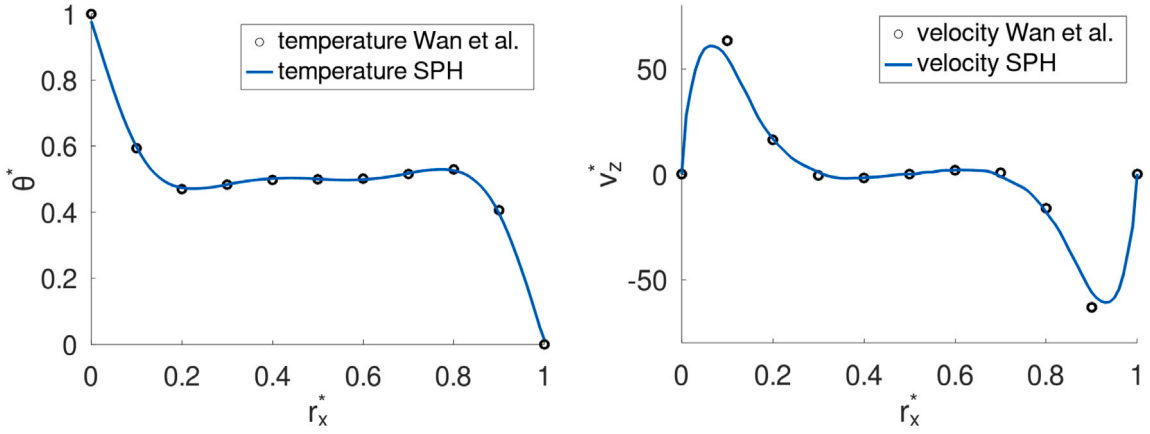

Fig. 13. Temperature (θ^*, left) and vertical velocity component (v_z^*, right) plots along a horizontal line through the centre of the cavity for the quasi-2D case, compared with the results of Wan et al. [59]. CFL number 0.1, $h = 2.0dp$, 20 particles in periodic dimension.

run successfully at the coarsest resolution. However, the flow becomes stationary before reaching the correct steady state for this largest particle spacing. Fig. 7 shows that the velocity is converging at between first and second order before the rate of convergence begins to decrease. Since the ratio $\frac{h}{dp}$ remains constant for all resolutions, a plateau is found as resolution is increased as the limiting discretisation error is reached [57].

Although the size of the error in temperature is smaller than for velocity, due to the no-slip boundary method, the limit of convergence is reached at a larger particle spacing and the error increases with the finest resolution. The limit is reached sooner since the computation of temperature involves the approximation of a second order gradient, which introduces an extra error. Wan et al. [59] also found that temperature converged faster with time than velocity, in agreement with these results. A coarsest resolution of $dp = 0.0005$ m was found for circulation to develop successfully and be sustained, without dissipation dominating the flow.

Fig. 8 shows the new adiabatic boundary condition from Eq. (19) is effective, and compares well to the isotherms found by Wan et al. [59]. Isotherms are normal to the adiabatic boundaries as they approach, since there is no change in temperature through them.

The Nusselt number, defined as

$$Nu = \left| \frac{\partial \theta^*}{\partial r_x^*} \right|_{r_z \in \text{wall}(\theta_H)} \tag{37}$$

is shown in Fig. 9. The gradient is calculated using a second order forward finite difference, which matches the best possible order of accuracy of the SPH method, with $\Delta x = dp$. There is overall agreement, however the maximum value of the Nusselt number is slightly overpredicted at the base the domain. The mean $\overline{\text{Nu}}$ at the hot wall is plotted against time in Fig. 10 where it is clear that the solution reaches steady state by $t^* = 0.3$.

3.3. Quasi-2D differentially heated cavity

To validate the code in three dimensions, a quasi-2D case is run by extending the domain into the third lateral dimension (the y direction) using periodic boundaries. In this 3-D domain, the width of the y-direction is set to be sufficiently small such that behaviour of the solution is effectively 2-D at the same time as being wide enough for a particle's kernel not to overlap with itself. Any slice of the $x - z$ plane can therefore be compared to the previous two dimensional cases. The case is run as previously, by specifying the number of particles in the lateral periodic y–dimension such that periodicity is achieved without particles' kernels interacting with themselves in order to prevent unphysical periodic effects. Hence, with an $h/dp = 2.5$ a minimum of 10 particles is required in the y–dimension. A finer resolution of $dp = 0.00025$ m is used, since the simulation is more sensitive to numerical dissipation with the extra dimension included and does not run successfully for $dp = 0.0005$ m since this leads to unphysical overlapping of kernels in the periodic y direction. The results in Fig. 11 show the comparison of temperature and velocity with the benchmark literature data.

Increasing the depth in the y–dimension to 20 SPH particles significantly increases runtime by more than 13 times, as can be seen for an example case in Table 3. In order to mitigate this, the smoothing length is set to $h = 1.5dp$ to maintain approximately the same number of neighbours as the 2D case, and the CFL number is increased from 0.1 to 0.2. The results in Fig. 12 are poorer because of these compromises, but this demonstrates the capability of running the case with a smaller smoothing length as a result of the extra dimension increasing particle numbers within the kernel. It is possible that the difference is also due to 3D effects, which accumulate with time. Although results are close for this smaller smoothing length, the exponential part of the temperature curve is not captured in Fig. 12.

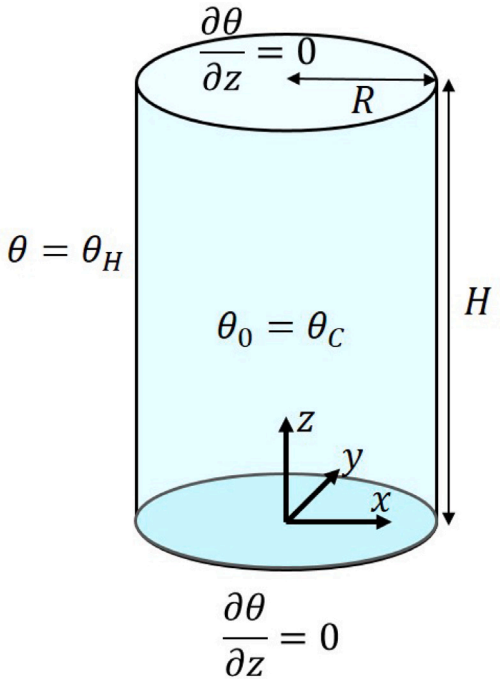

Fig. 14. Three-dimensional cylindrical tank with a single fluid component.

Thus, it is clear that a large smoothing length, h, is required in three dimensions, as well as two dimensions, in order to get accurate results. The smoothing length $h = 2.0dp$, as was successful for two dimensions, is chosen, but the domain is extended to 20 particles in the periodic dimension. This larger smoothing length gives significantly better results, in Fig. 13, than the previous h. Increasing the number of neighbours in this way is shown to improve results and get very close to the benchmark solution of Wan et al. [59]. To reduce runtime without impacting accuracy, it may be possible to increase the CFL number, since the simulation is stable.

3.4. Convective flow in a cylindrical tank

3.4.1. Single-component 3-D convective flow

A case of flow within a cylindrical tank, where the curved surface is heated, is proposed. Initially, a single component fluid completely fills the tank. As can be seen in Fig. 14, the top and bottom boundaries are adiabatic. This is enforced by the new mDBC adiabatic boundary condition for temperature, defined in Eq. (19). Boundary conditions for density and velocity are enforced using DBC, as particles were found to escape through the boundaries when using mDBC. The number of fluid particles penetrating the boundary is significantly reduced when using the DBC, suggesting a correction needs to be made to the mDBC method to take account of the difference in volume when extrapolating density into a concave boundary. The curved boundary is held at constant temperature θ_H, heating the fluid inside the container. The fluid has a uniform initial temperature of θ_C.

Beginning with the parameters used in Section 3.2, where the fluid is air with a constant viscosity of $\nu = 1.506\times10^{-5}$ m^2 s^{-1}, and also setting $H = 2R = 0.0386$ m, a similar Rayleigh number ($Ra = 10^5$) is expected. The temperatures are also chosen to be the same, with $\theta_C = 283$ K and $\theta_H = 303$ K. All boundaries have the same thermal properties as the fluid and the initial particle spacing is chosen to be $dp = 0.001$ m.

Density diffusion is included to reduce accumulation of numerical error from pressure fluctuations, and particle shifting has typical coefficient $D = -2$ to maintain a uniform particle distribution. This work

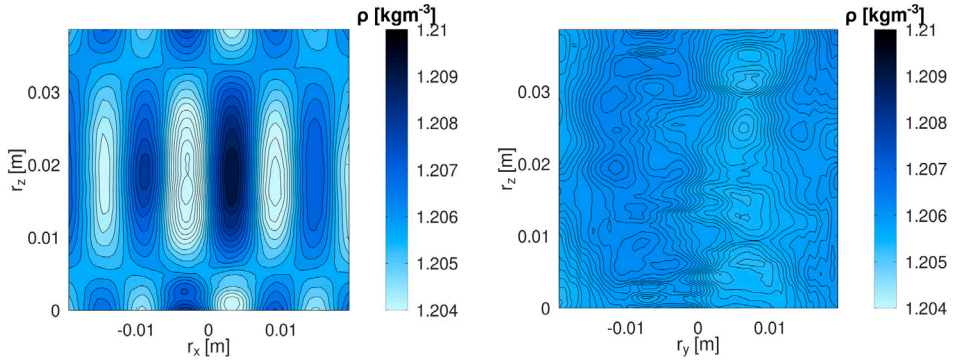

Fig. 15. Density in $x = 0$ and $y = 0$ planes at $t = 45$ s for single component cylindrical tank.

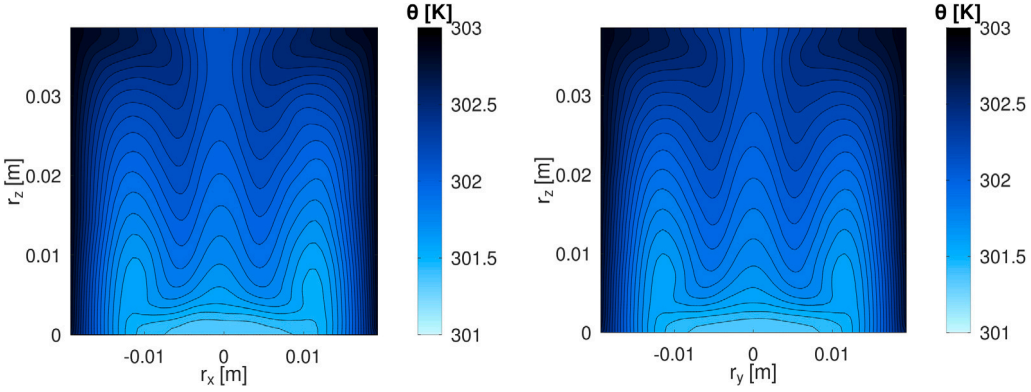

Fig. 16. Temperature in $x = 0$ and $y = 0$ planes at $t = 45$ s for single component cylindrical tank.

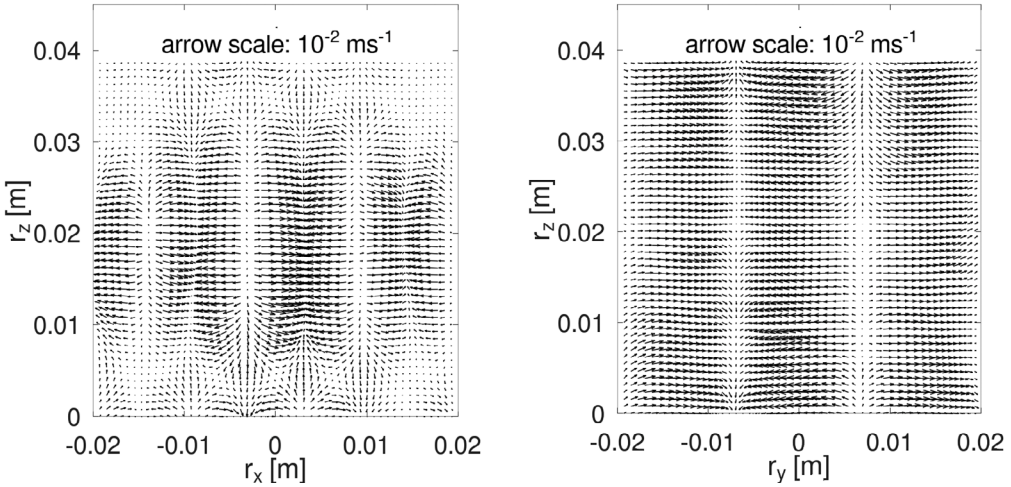

Fig. 17. Velocity in $x = 0$ and $y = 0$ planes at $t = 45$ s for single component cylindrical tank.

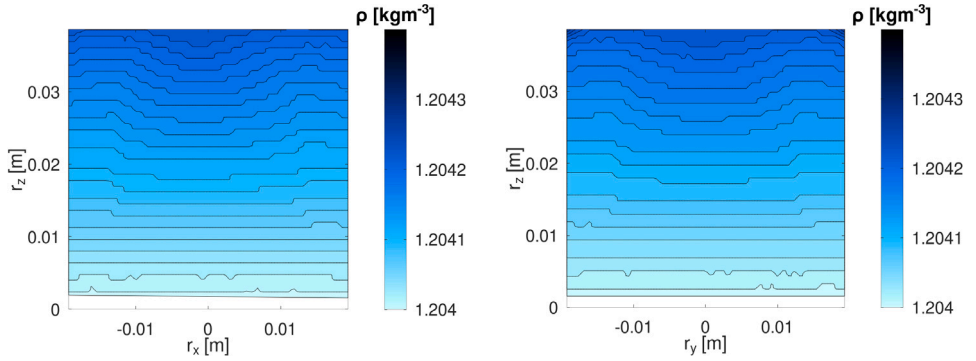

Fig. 18. Density in $x = 0$ and $y = 0$ planes at $t = 45$ s for single component cylindrical tank but increased viscosity.

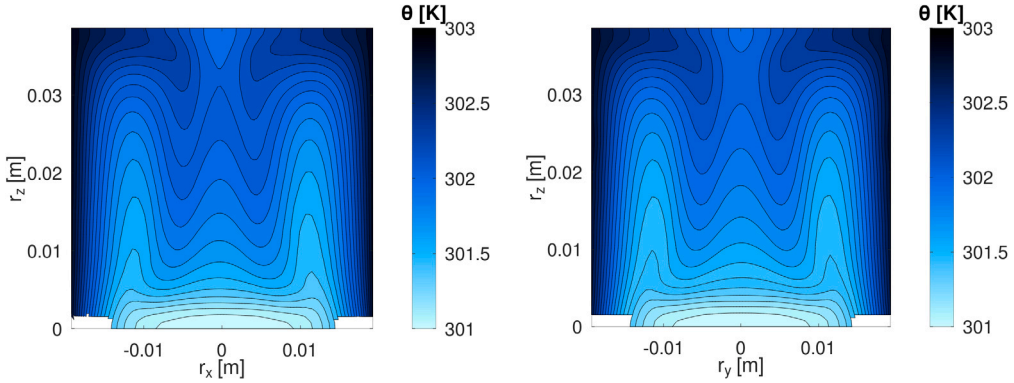

Fig. 19. Temperature in $x = 0$ and $y = 0$ planes at $t = 45$ s for single component cylindrical tank but increased viscosity.

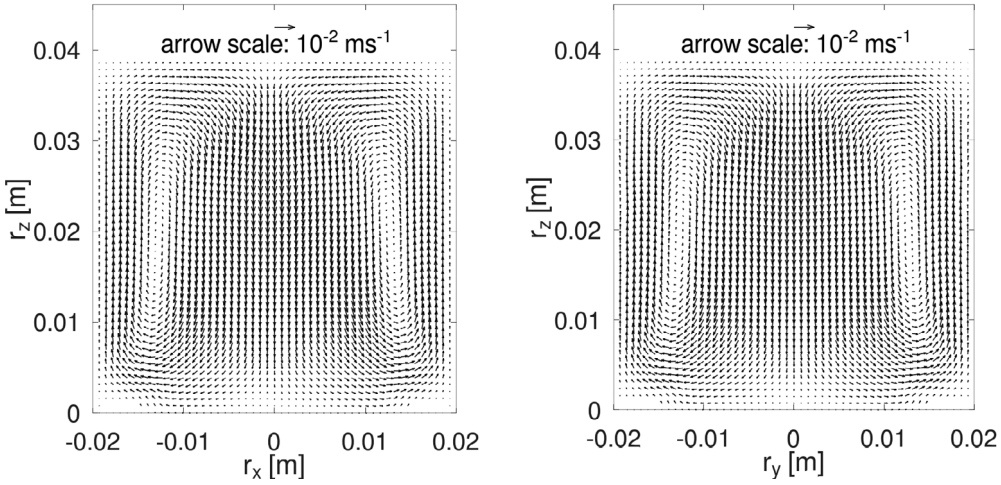

Fig. 20. Velocity in $x = 0$ and $y = 0$ planes at $t = 45$ s for single component cylindrical tank but increased viscosity.

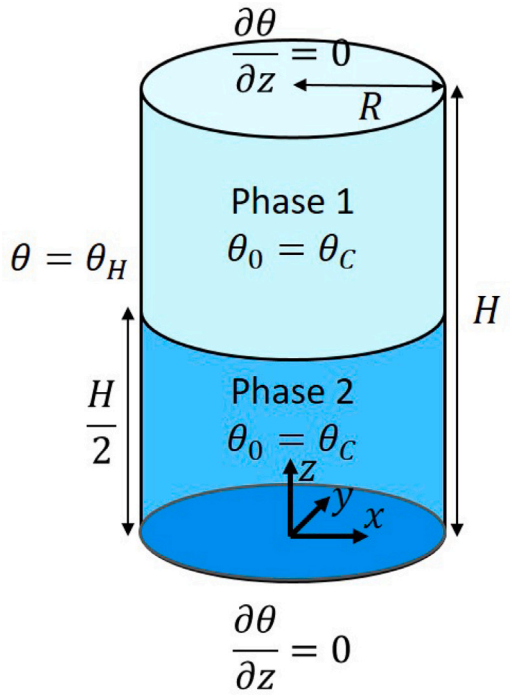

Fig. 21. Thee-dimensional vitrification case with two fluid components.

uses the shifting term of Skillen et al.[66],

$$\delta\mathbf{r}_i = -Dh|\mathbf{v}_i|dt\sum_j \frac{m_j}{\rho_j}\nabla_i W_{ij}. \tag{38}$$

The density diffusion term of Fourtakas et al. [67], included in DualSPHysics v5.0, is used for this case with density diffusion term

$$\delta hc\sum_j 2\frac{m_j}{\rho_j}(\rho_{ij} - \rho_{ij}^H)\frac{\mathbf{r}_{ij}}{r_{ij}^2}\cdot\nabla_i W_{ij}. \tag{39}$$

The variables at 45 s in planes $x = 0$ and $y = 0$ are displayed in Figs. 15–17, where properties have been interpolated to a regular grid of spacing equal to the initial interparticle distance. It can be seen in Fig. 16 that heating is clearly taking place via conduction from the curved wall where temperatures are increased and convection of the fluid resulting in heat transferring towards the centre of the tank at the top. However, the density in Fig. 15 is not radially symmetric as expected, with velocity in Fig. 17 behaving similarly. No relevant literature could be found to determine whether this is an appearance of circulation cells due to a physical instability. Later, around 60 s, particles are lost when pre-defined density limits are exceeded.

Increasing the constant viscosity from $\nu = 1.506\times10^{-5}$ m^2 s^{-1} to $\nu = 10^{-4}$ m^2 s^{-1} to avoid the density pattern found previously results in a symmetric density as well as velocities clearly following convective flow, as seen in Figs. 18–20. This results in heating throughout the cavity and evidence of recirculation, with all particles having an increased temperature at 45 s. A single fluid component within the heated cylindrical tank exhibits radially symmetric circulation due to buoyancy-driven flow.

3.4.2. Multi-component 3-D convective flow

Mixing of components is investigated by splitting the fluid within the cavity horizontally into two fluid components of equal height. This is shown in Fig. 21, where boundary conditions remain as before.

Starting from the previous case with dimensions $H = 2R = 0.0386$ m, each phase has a constant viscosity. The top fluid component is chosen to have $\nu_1 = 2\times10^{-4}$ m^2 s^{-1} and the bottom $\nu_2 = 10^{-4}$ m^2 s^{-1}. Other fluid properties are the same as for the previous single-component case. Both temperature and density are radially symmetric in Figs. 22 and 23, but temperature has almost reached θ_H everywhere by 60 s. Since viscosity is constant in each fluid component, Fig. 24 shows clear movement of and mixing between components caused by convective flow. This is confirmed by the velocity field in Fig. 25.

Previous work by the authors [44] evaluated multiple numerical measures of mixing and proposed a new measure that can quantify both local composition and movement within the mixture. A summary of the measures assessed [44] is shown in Table 4. The new measure combines volume fraction and finite time Lyapunov exponent to illustrate and quantify both the degree of mixing at a point, as well as how well-mixed the components are at that location. Here, the measures are applied to gain insight into mixing taking place within the cavity. The finite-time Lyapunov exponent (FTLE) in Fig. 26 shows convective flow and circulation, whilst mixing between components is seen in the other measures. The interface between components is highlighted, and large areas of each isolated component fluid shown. Both mixing entropy (both components) and the global mixing measure in Fig. 27 show mixing increasing with time. By 120 s the rate of increase is slowing, but a steady state has not yet been reached.

The three-dimensional mixing behaviour can be seen by plotting an isosurface of the combined mixing measure, as in Fig. 28. The mixing measure is computed for all points in the three-dimensional region where SPH particles were at time $t = 0$ s, showing convective flow driven by the heated wall. Investigating a range of isosurface values shows that fluid initially at the centre of the tank has relatively high VF-FTLE values and therefore good mixing, with the lowest levels of mixing occurring towards the bottom of the tank.

3.4.3. Multi-component 2-D convective flow

Assuming radial symmetry of flow and variables within the tank, a two-dimensional plane at $y = 0$ is simulated, as shown in Fig. 29 with $\nu_1 = 2\times10^{-4}$ m^2 s^{-1}, $\nu_2 = 10^{-4}$ m^2 s^{-1}. Running two-dimensional simulations allows a general understanding of a large number of cases to be obtained by taking advantage of the shorter runtime whilst providing insight into the flow behaviour. The results at 300 s in Fig. 30 show the same flow behaviours, in particular the circulation caused by heating at both side walls and symmetry of density and temperature. Particles are still lost, but fewer at 7% over 300 s.

The effect of this circulation on mixing between components is demonstrated in Fig. 31. The volume fraction (VF) clearly shows that the convection is causing circulation and mixing of component fluid, although there are still regions of separate components at 300 s. The FTLE is fairly constant for all times, consisting of the two circulating cells. Robinson's measure shows clearly the interface between components, whereas the new mixing measure has more variation at the interface depending on where it lies on areas of high circulation. The flow behaviour closely resembles the three-dimensional case, justifying the use of two-dimensional simulations in preliminary investigations.

4. Conclusions

This paper has presented a new implementation of an adiabatic SPH boundary condition with buoyancy to simulate buoyancy-driven circulation in multi-component flows. The temperature equation (Eq. (9)) and Boussinesq approximation (Eq. (15)) are added to simulate buoyancy-driven flow in the differentially heated cavity case in Section 3.2. The Dirichlet boundary condition for temperature, discussed in Section 2.3, is found to be adequate for heating. However, the new higher order adiabatic boundary condition, based on the mDBC method, is established to be superior to the more simple method of excluding boundary contributions. The thermal mDBC approach has been validated against a range of test cases, specifically different types of differentially-heated cavities, where it is shown to produce

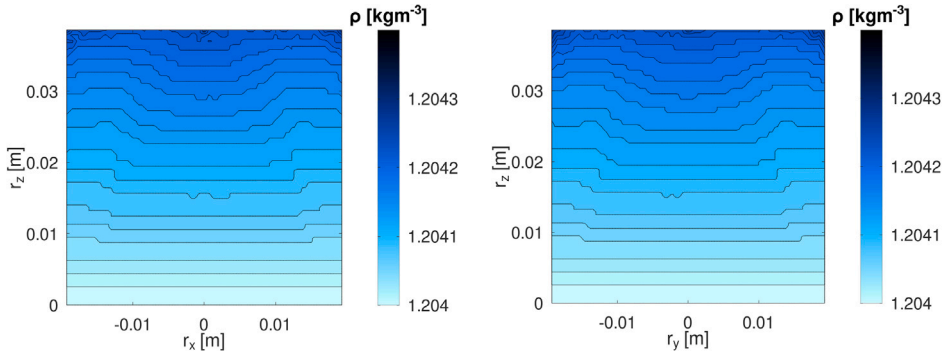

Fig. 22. Density in $x = 0$ and $y = 0$ planes at 60 s for two-component cylindrical tank.

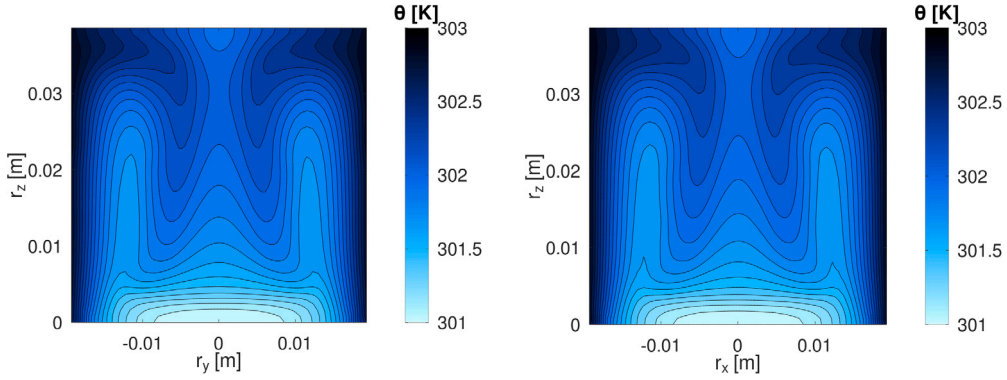

Fig. 23. Temperature in $x = 0$ and $y = 0$ planes at 60 s for two-component cylindrical tank.

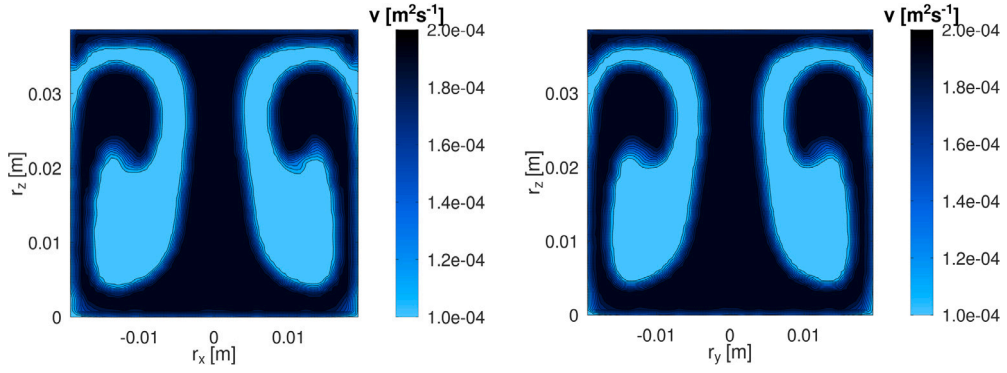

Fig. 24. Viscosity in $x = 0$ and $y = 0$ planes at 60 s for two-component cylindrical tank.

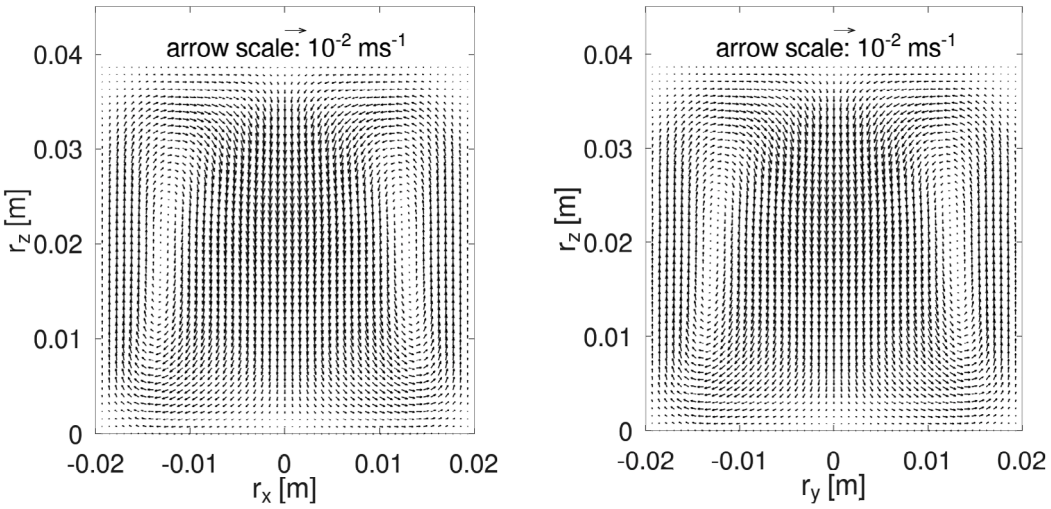

Fig. 25. Velocity in $x = 0$ and $y = 0$ planes at 60 s for two-component cylindrical tank.

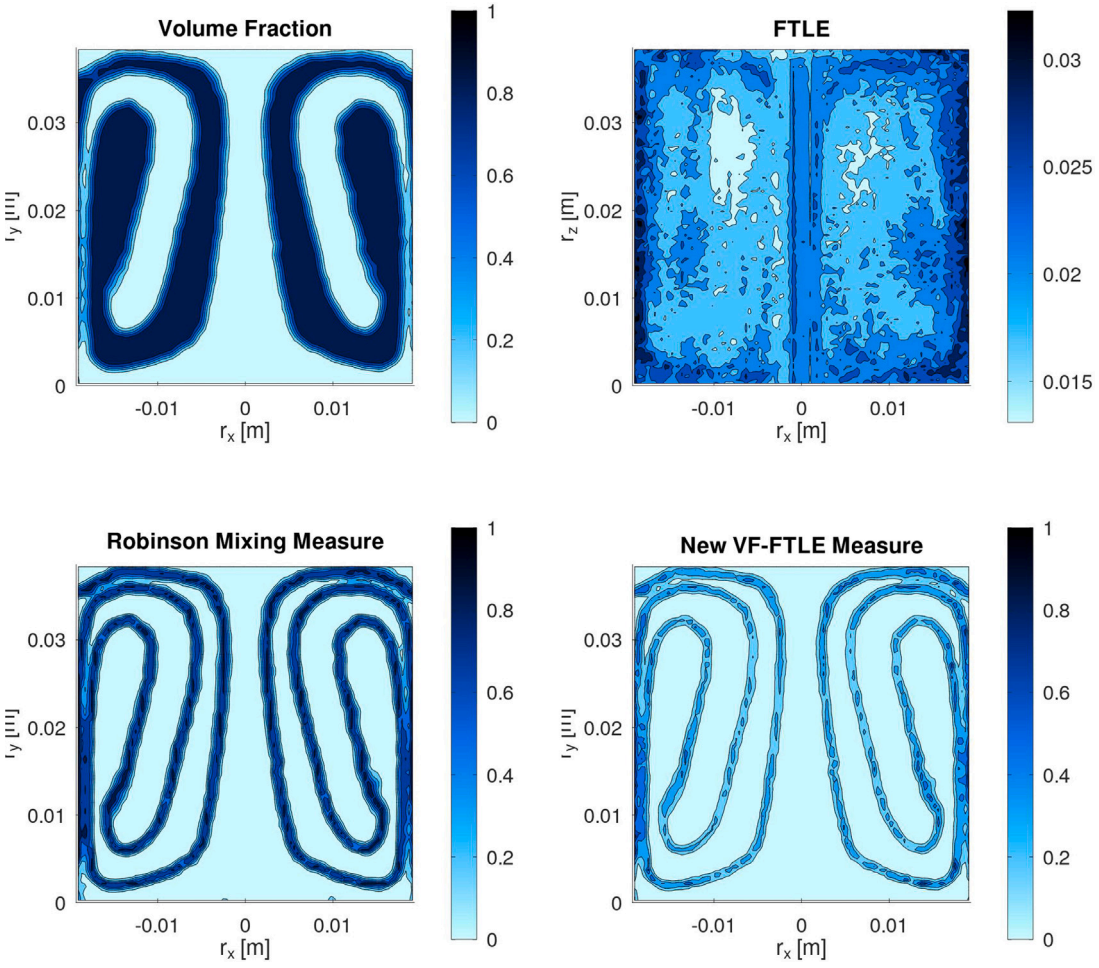

Fig. 26. Mixing measures at 120 s for three-dimensional two-component cylindrical tank.

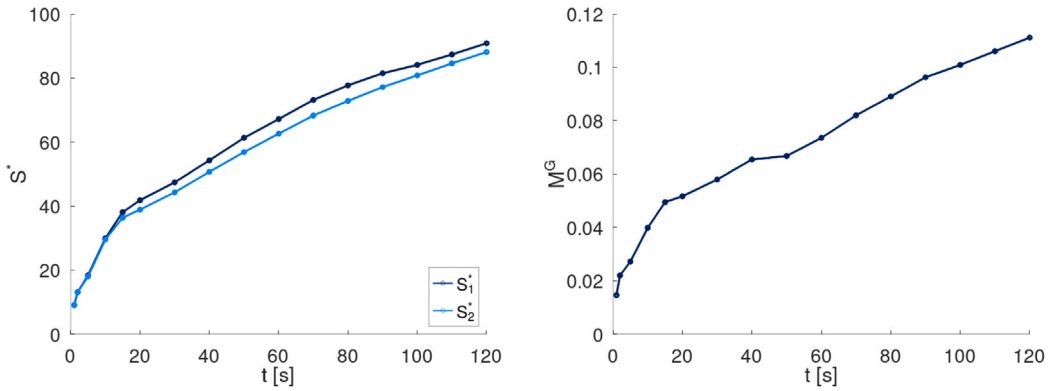

Fig. 27. Global mixing measures plotted against time for three-dimensional two-component cylindrical tank.

Fig. 28. Isosurface of new VF-FTLE mixing measure M at value 0.01 for convective flow in a cylindrical tank.

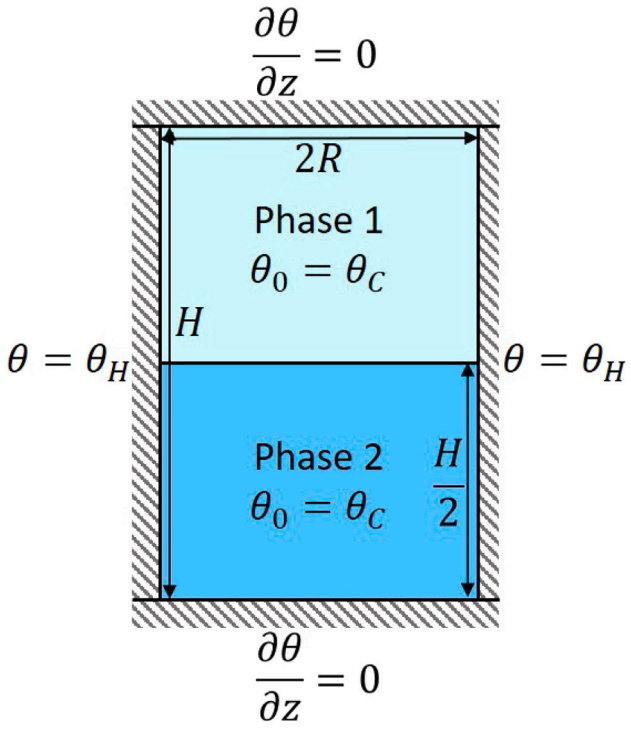

Fig. 29. Two-dimensional heated cylindrical tank with two fluid components.

satisfactory agreement with reference solutions as long as the ratio of the smoothing length to particle size is sufficiently large.

The cases in Section 3.4 demonstrate buoyancy-driven circulation within a cylindrical tank heated at the curved wall. When two fluid components are present, the flow causes gradual mixing between the components. The mixing measure combining the volume fraction (VF) and finite time Lyapunov exponent (FTLE) allows us to see in detail the mixing in a 3-D cylindrical tank providing more detailed insight into mixing than using either the velocity field or just the VF or FTLE alone. Local mixing measures show the movement of fluid components, while the distinctions of the new VF-FTLE measure are accentuated where the regions of high circulation are located. The global mixing measures give insight into the overall degree of mixing achieved at an instant, as well as the progress towards homogeneity over time.

CRediT authorship contribution statement

Georgina Reece: Writing – original draft, Visualization, Validation, Software, Methodology, Investigation, Formal analysis, Conceptualization. **Benedict D. Rogers:** Writing – review & editing, Supervision, Methodology, Conceptualization. **Georgios Fourtakas:** Writing – review & editing, Supervision, Methodology, Conceptualization. **Steven Lind:** Writing – review & editing, Supervision, Methodology, Conceptualization.

Declaration of competing interest

The authors declare the following financial interests/personal relationships which may be considered as potential competing interests: Georgina Reece reports financial support was provided by Engineering and Physical Sciences Research Council. Georgina Reece reports financial support was provided by National Nuclear Laboratory. If there are other authors, they declare that they have no known competing financial interests or personal relationships that could have appeared to influence the work reported in this paper.

Data availability

Data will be made available on request.

Acknowledgements

The work was supported by the EPSRC and National Nuclear Laboratory [Grant No. 1961431]. The authors would also like to acknowledge the assistance given by Research IT and the use of the Computational Shared Facility at the University of Manchester.

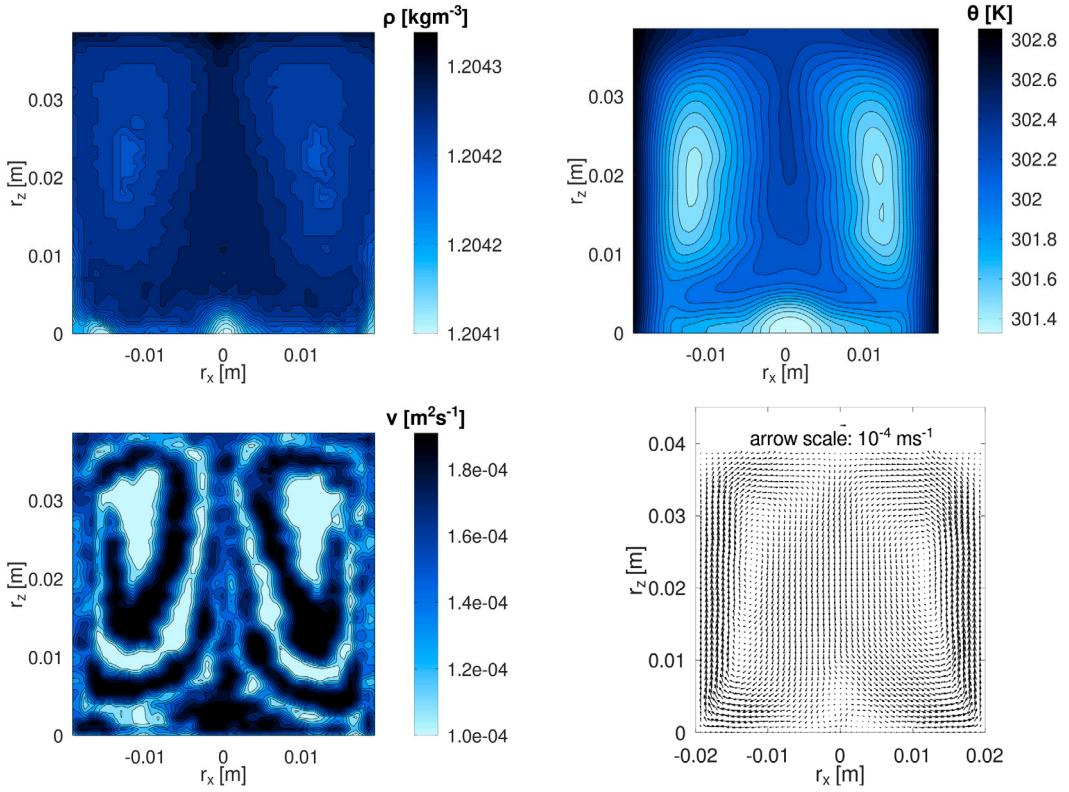

Fig. 30. Density, temperature, viscosity and velocity at 300 s for two-dimensional two-component cylindrical tank.

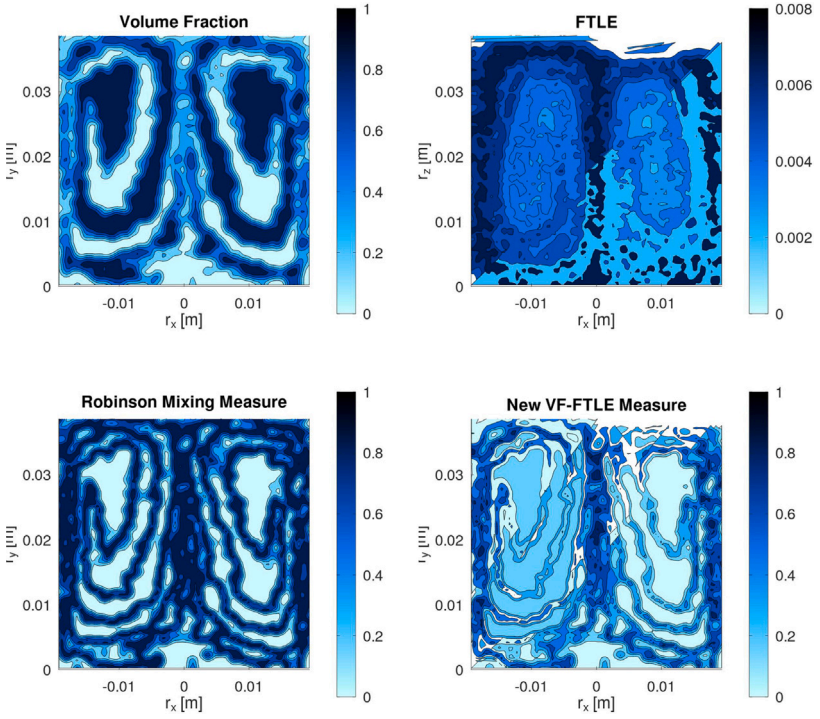

Fig. 31. Mixing measures at 300 s for two-dimensional two-component cylindrical tank.

References

[1] G. Batchelor, Heat transfer by free convection across a closed cavity between vertical boundaries at different temperatures, Quart. Appl. Math. 12 (3) (1954) 209–233.

[2] G.K. Batchelor, V.M. Canuto, J.R. Chasnov, Homogeneous buoyancy-generated turbulence, J. Fluid Mech. 235 (1992) 349–378, http://dx.doi.org/10.1017/S0022112092001149.

[3] C.H. Bosanquet, G. Horn, M.W. Thring, G.I. Taylor, The effect of density differences on the path of jets, Proc. R. Soc. Lond. Ser. A. Math. Phys. Sci. 263 (1314) (1961) 340–352, http://dx.doi.org/10.1098/rspa.1961.0164.

[4] D. Livescu, J.R. Ristorcelli, Buoyancy-driven variable-density turbulence, J. Fluid Mech. 591 (2007) 43–71, http://dx.doi.org/10.1017/S0022112007008270.

[5] A. Lefauve, P.F. Linden, Buoyancy-driven exchange flows in inclined ducts, J. Fluid Mech. 893 (2020) A2, http://dx.doi.org/10.1017/jfm.2020.212.

[6] P. Le Quéré, M. Behnia, From onset of unsteadiness to chaos in a differentially heated square cavity, J. Fluid Mech. 359 (1998) 81–107, http://dx.doi.org/10.1017/S0022112097008458.

[7] R. Kumar, A. Dewan, A study of LES-SGS closure models applied to a square buoyant cavity, Int. J. Heat Mass Transfer 98 (2016) 164–175, http://dx.doi.org/10.1016/j.ijheatmasstransfer.2016.02.057.

[8] C. Panwisawas, C. Qiu, Y. Sovani, J. Brooks, M. Attallah, H. Basoalto, On the role of thermal fluid dynamics into the evolution of porosity during selective laser melting, Scr. Mater. 105 (2015) 14–17, http://dx.doi.org/10.1016/j.scriptamat.2015.04.016.

[9] G.-R. Liu, M.B. Liu, Smoothed Particle Hydrodynamics: a Meshfree Particle Method, World Scientific, 2003.

[10] K. Khanafer, S. Aithal, K. Vafai, Mixed convection heat transfer in a differentially heated cavity with two rotating cylinders, Int. J. Therm. Sci. 135 (2019) 117–132, http://dx.doi.org/10.1016/j.ijthermalsci.2018.07.020.

[11] H. Tang, L.C. Wrobel, Modelling the interfacial flow of two immiscible liquids in mixing processes, Internat. J. Engrg. Sci. 43 (15–16) (2005) 1234–1256.

[12] P. Yang, C. Huang, Z. Zhang, T. Long, M. Liu, Simulating natural convection with high Rayleigh numbers using the smoothed particle hydrodynamics method, Int. J. Heat Mass Transfer 166 (2021) 120758.

[13] F.H. Harlow, PIC and its progeny, Comput. Phys. Comm. 48 (1) (1988) 1–10.

[14] R.A. Gingold, J.J. Monaghan, Smoothed particle hydrodynamics: Theory and application to non-spherical stars, Mon. Not. R. Astron. Soc. 181 (3) (1977) 375–389.

[15] L.B. Lucy, A numerical approach to the testing of the fission hypothesis, Astron. J. 82 (1977) 1013–1024.

[16] D. Violeau, B.D. Rogers, Smoothed particle hydrodynamics (SPH) for free-surface flows: Past, present and future, J. Hydraul. Res. 54 (1) (2016) 1–26.

[17] T. Ye, D. Pan, C. Huang, M. Liu, Smoothed particle hydrodynamics (SPH) for complex fluid flows: Recent developments in methodology and applications, Phys. Fluids 31 (1) (2019) 011301.

[18] M.S. Shadloo, G. Oger, D. Le Touzé, Smoothed particle hydrodynamics method for fluid flows, towards industrial applications: Motivations, current state, and challenges, Comput. & Fluids 136 (2016) 11–34.

[19] Z.-B. Wang, R. Chen, H. Wang, Q. Liao, X. Zhu, S.-Z. Li, An overview of smoothed particle hydrodynamics for simulating multiphase flow, Appl. Math. Model. 40 (23) (2016) 9625–9655, http://dx.doi.org/10.1016/j.apm.2016.06.030.

[20] J.J. Monaghan, Smoothed particle hydrodynamics, Annu. Rev. Astron. Astrophys. 30 (1) (1992) 543–574.

[21] S.J. Lind, P.K. Stansby, B.D. Rogers, Incompressible–compressible flows with a transient discontinuous interface using smoothed particle hydrodynamics (SPH), J. Comput. Phys. 309 (2016) 129–147.

[22] H. Gotoh, A. Khayyer, Current achievements and future perspectives for projection-based particle methods with applications in ocean engineering, J. Ocean Eng. Mar. Energy 2 (2016) 251–278.

[23] M. Luo, A. Khayyer, P. Lin, Particle methods in ocean and coastal engineering, Appl. Ocean Res. 114 (2021) 102734.

[24] M. Robinson, P.W. Cleary, The influence of cam geometry and operating conditions on chaotic mixing of viscous fluids in a twin cam mixer, AIChE J. 57 (3) (2011) 581–598.

[25] M. Robinson, P. Cleary, J. Monaghan, Analysis of mixing in a twin cam mixer using smoothed particle hydrodynamics, AIChE J. 54 (8) (2008) 1987–1998.

[26] P.W. Cleary, Modelling confined multi-material heat and mass flows using SPH, Appl. Math. Model. 22 (12) (1998) 981–993.

[27] P.W. Cleary, J.J. Monaghan, Conduction modelling using smoothed particle hydrodynamics, J. Comput. Phys. 148 (1) (1999) 227–264.

[28] L. Brookshaw, The Stability of Binary Systems and Rotating Stars (Ph.D. thesis), Monash University, 1986.

[29] K. Szewc, J. Pozorski, A. Taniere, Modeling of natural convection with smoothed particle hydrodynamics: non-Boussinesq formulation, Int. J. Heat Mass Transfer 54 (23–24) (2011) 4807–4816.

[30] X. Yang, S.-C. Kong, Numerical study of natural convection in a horizontal concentric annulus using smoothed particle hydrodynamics, Eng. Anal. Bound. Elem. 102 (2019) 11–20.

[31] A. Leroy, D. Violeau, M. Ferrand, A. Joly, Buoyancy modelling with incompressible SPH for laminar and turbulent flows, Internat. J. Numer. Methods Fluids 78 (8) (2015) 455–474.

[32] R. Rook, M. Yildiz, S. Dost, Modeling transient heat transfer using SPH and implicit time integration, Num. Heat Transf. Part B: Fund. 51 (1) (2007) 1–23.

[33] K.C. Ng, Y.L. Ng, T.W.H. Sheu, A. Alexiadis, Assessment of smoothed particle hydrodynamics (SPH) models for predicting wall heat transfer rate at complex boundary, Eng. Anal. Bound. Elem. 111 (2020) 195–205.

[34] S. Adami, X.Y. Hu, N.A. Adams, A generalized wall boundary condition for smoothed particle hydrodynamics, J. Comput. Phys. 231 (21) (2012) 7057–7075, http://dx.doi.org/10.1016/j.jcp.2012.05.005.

[35] M.A.E. Sikarudi, A.H. Nikseresht, Neumann and Robin boundary conditions for heat conduction modeling using smoothed particle hydrodynamics, Comput. Phys. Comm. 198 (2016) 1–11.

[36] J. Wang, W. Hu, X. Zhang, W. Pan, Modeling heat transfer subject to inhomogeneous Neumann boundary conditions by smoothed particle hydrodynamics and peridynamics, Int. J. Heat Mass Transfer 139 (2019) 948–962, http://dx.doi.org/10.1016/j.ijheatmasstransfer.2019.05.054.

[37] H.F. Schwaiger, An implicit corrected SPH formulation for thermal diffusion with linear free surface boundary conditions, Internat. J. Numer. Methods Engrg. 75 (6) (2008) 647–671.

[38] S.J. Cummins, M. Rudman, An SPH projection method, J. Comput. Phys. 152 (2) (1999) 584–607.

[39] A. Mayrhofer, B.D. Rogers, D. Violeau, M. Ferrand, Investigation of wall bounded flows using SPH and the unified semi-analytical wall boundary conditions, Comput. Phys. Comm. 184 (11) (2013) 2515–2527.

[40] J.C. Joubert, D.N. Wilke, N. Govender, P. Pizette, U. Tuzun, N.-E. Abriak, 3D gradient corrected SPH for fully resolved particle–fluid interactions, Appl. Math. Model. 78 (2020) 816–840.

[41] B. Bai, D. Rao, T. Xu, P. Chen, SPH-FDM boundary for the analysis of thermal process in homogeneous media with a discontinuous interface, Int. J. Heat Mass Transfer 117 (2018) 517–526.

[42] J.M. Domínguez, G. Fourtakas, C. Altomare, R.B. Canelas, A. Tafuni, O. García-Feal, I. Martínez-Estévez, A. Mokos, R. Vacondio, A.J.C. Crespo, et al., DualSPHysics: From fluid dynamics to multiphysics problems, Comput. Part. Mech. 9 (2022) 867–895.

[43] A. English, J.M. Domínguez, R. Vacondio, A.J.C. Crespo, P.K. Stansby, S.J. Lind, L. Chiapponi, M. Gómez-Gesteira, Modified dynamic boundary conditions (mDBC) for general-purpose smoothed particle hydrodynamics (SPH): application to tank sloshing, dam break and fish pass problems, Comput. Part. Mech. (2021) 1–15.

[44] G. Reece, B.D. Rogers, S. Lind, G. Fourtakas, New instability and mixing simulations using SPH and a novel mixing measure, J. Hydrodyn. 32 (4) (2020) 684–698.

[45] H. Wendland, Piecewise polynomial, positive definite and compactly supported radial functions of minimal degree, Adv. Comput. Math. 4 (1) (1995) 389–396.

[46] W. Dehnen, H. Aly, Improving convergence in smoothed particle hydrodynamics simulations without pairing instability, Mon. Not. R. Astron. Soc. 425 (2) (2012) 1068–1082.

[47] J.J. Monaghan, Simulating free surface flows with SPH, J. Comput. Phys. 110 (2) (1994) 399–406.

[48] J.P. Morris, P.J. Fox, Y. Zhu, Modeling low Reynolds number incompressible flows using SPH, J. Comput. Phys. 136 (1) (1997) 214–226.

[49] J.B. Avalos, M. Antuono, A. Colagrossi, A. Souto-Iglesias, Shear-viscosity-independent bulk-viscosity term in smoothed particle hydrodynamics, Phys. Rev. E 101 (1) (2020) 013302.

[50] J.J. Monaghan, R.A. Gingold, Shock simulation by the particle method SPH, J. Comput. Phys. 52 (2) (1983) 374–389, http://dx.doi.org/10.1016/0021-9991(83)90036-0.

[51] Z.-G. Feng, M.C. Ponton, Smoothed particle method for studying heat and mass transfer between fluid and solid, in: ASME 2014 International Mechanical Engineering Congress and Exposition, American Society of Mechanical Engineers, 2014, V08BT10A018.

[52] A.K. Das, P.K. Das, Modeling of liquid–vapor phase change using smoothed particle hydrodynamics, J. Comput. Phys. 303 (2015) 125–145.

[53] S. Marrone, M. Antuono, A. Colagrossi, G. Colicchio, D. Le Touzé, G. Graziani, δ-SPH model for simulating violent impact flows, Comput. Methods Appl. Mech. Engrg. 200 (13–16) (2011) 1526–1542.

[54] M.B. Liu, G.-R. Liu, Restoring particle consistency in smoothed particle hydrodynamics, Appl. Numer. Math. 56 (1) (2006) 19–36.

[55] G. Fourtakas, B.D. Rogers, Modelling multi-phase liquid-sediment scour and resuspension induced by rapid flows using smoothed particle hydrodynamics (SPH) accelerated with a graphics processing unit (GPU), Adv. Water Resour. 92 (2016) 186–199.

[56] G. Reece, Modelling and Investigation of Multi-Phase Mixing for Vitrification Applications using Smoothed Particle Hydrodynamics (SPH) (Ph.D. thesis), The University of Manchester, Manchester, UK, 2022.

[57] N.J. Quinlan, M. Basa, M. Lastiwka, Truncation error in mesh-free particle methods, Internat. J. Numer. Methods Engrg. 66 (13) (2006) 2064–2085.

[58] G. de Vahl Davis, Natural convection of air in a square cavity: A bench mark numerical solution, Internat. J. Numer. Methods Fluids 3 (3) (1983) 249–264.
[59] D.C. Wan, B.S.V. Patnaik, G.W. Wei, A new benchmark quality solution for the buoyancy-driven cavity by discrete singular convolution, Num. Heat Transf.: Part B: Fund. 40 (3) (2001) 199–228.
[60] G. Barakos, E. Mitsoulis, D.O. Assimacopoulos, Natural convection flow in a square cavity revisited: Laminar and turbulent models with wall functions, Internat. J. Numer. Methods Fluids 18 (7) (1994) 695–719.
[61] M. Antuono, A. Colagrossi, S. Marrone, Numerical diffusive terms in weakly-compressible SPH schemes, Comput. Phys. Comm. 183 (12) (2012) 2570–2580.
[62] N. Massarotti, P. Nithiarasu, O. Zienkiewicz, Characteristic-based-split (CBS) algorithm for incompressible flow problems with heat transfer, Internat. J. Numer. Methods Heat Fluid Flow 8 (8) (1998) 969–990.
[63] M. Manzari, An explicit finite element algorithm for convection heat transfer problems, Internat. J. Numer. Methods Heat Fluid Flow 9 (8) (1999) 860–877.
[64] B. Tóth, K. Szabó, Flow structure detection with smoothed particle hydrodynamics, in: D. Violeau, A. Hérault, A. Joly (Eds.), Proceedings of the 9th International SPHERIC Workshop, 2014.
[65] T.G. Kang, S. Ahn, S.H. Chung, S.T. Chung, Y.S. Kwon, S.J. Park, R.M. German, 9 - modeling and simulation of metal injection molding (MIM), in: D.F. Heaney (Ed.), Handbook of Metal Injection Molding, in: Woodhead Publishing Series in Metals and Surface Engineering, Woodhead Publishing, 2012, pp. 197–236e, http://dx.doi.org/10.1533/9780857096234.2.197.
[66] A. Skillen, S. Lind, P.K. Stansby, B.D. Rogers, Incompressible smoothed particle hydrodynamics (SPH) with reduced temporal noise and generalised Fickian smoothing applied to body–water slam and efficient wave–body interaction, Comput. Methods Appl. Mech. Engrg. 265 (2013) 163–173.
[67] G. Fourtakas, J.M. Dominguez, R. Vacondio, B.D. Rogers, Local uniform stencil (LUST) boundary condition for arbitrary 3-D boundaries in parallel smoothed particle hydrodynamics (SPH) models, Comput. & Fluids 190 (2019) 346–361.